

# Global study of quadrupole correlation effects

M. Bender,<sup>1,2,3</sup> G. F. Bertsch,<sup>1</sup> and P.-H. Heenen<sup>4</sup>

<sup>1</sup>*Department of Physics and Institute for Nuclear Theory,  
Box 351560, University of Washington, Seattle, WA 98195*

<sup>2</sup>*Physics Division, Argonne National Laboratory, 9700 S. Cass Avenue, Argonne, IL 60439*

<sup>3</sup>*National Superconducting Cyclotron Laboratory, Michigan State University, East Lansing, MI 48824*

<sup>4</sup>*Service de Physique Nucléaire Théorique, Université Libre de Bruxelles, CP 229, B-1050 Brussels, Belgium*

(Dated: August 26 2005)

We discuss the systematics of ground-state quadrupole correlations of binding energies and mean-square charge radii for all even-even nuclei, from  $^{16}\text{O}$  up to the superheavies, for which data are available. To that aim we calculate their correlated  $J = 0$  ground state by means of the angular-momentum and particle-number projected generator coordinate method, using the axial mass quadrupole moment as the generator coordinate and self-consistent mean-field states only restricted by axial, parity, and time-reversal symmetries. The calculation is performed within the framework of a non-relativistic self-consistent mean-field model using the same non-relativistic Skyrme interaction SLy4 and a density-dependent pairing force to generate the mean-field configurations and mix them. The main conclusions of our study are: (i) The quadrupole correlation energy varies between a few 100 keV and about 5.5 MeV. It is affected by shell closures, but varies only slightly with mass and asymmetry. (ii) Projection on angular momentum  $J = 0$  provides the major part of the energy gain of up to about 4 MeV; all nuclei in the study including doubly magic gain energy by deformation. (iii) the mixing of projected states with different intrinsic axial deformation adds a few 100 keV up to 1.5 MeV to the correlation energy. (iv) Typically nuclei below mass  $A \leq 60$  have a larger correlation energy than static deformation energy while the heavier deformed nuclei have larger static deformation energy than correlation energy. (v) Inclusion of the quadrupole correlation energy improves the description of mass systematics, particularly around shell closures and for differential quantities, namely two-nucleon separation energies and two-nucleon gaps. The correlation energy provides an explanation of “mutually enhanced magicity”. (vi) The correlation energy tends to decrease the shell effect on binding energies around magic numbers, but the magnitude of the suppression is not large enough to explain the relative overbinding at  $N = 82$  and  $N = 126$  neutron shell closures in mean-field models. (vii) Charge radii are also found to be sensitive to the quadrupole correlations. Static quadrupole deformations lead to a significant improvement of the overall systematics of charge radii. The dynamical correlations improve the local systematics of radii, in particular around shell closures. Although the dynamical correlations might reduce the charge radii for specific nuclei, they lead to an overall increase of radii when included, in particular in light nuclei.

PACS numbers: 21.60.Jz, 21.10.Dr, 21.10.Ft

## I. INTRODUCTION

The last few years witnessed a tremendous progress toward the construction of microscopic models for nuclear masses. Most promising for such an endeavor is self-consistent mean-field theory (SCMF), also called density functional theory (DFT). See Ref. [1] for a recent review. Since the work of Tondeur *et al.* [2], fits of self-consistent mean-field models to all experimentally known masses have become available. However, the fits are only competitive with the *de facto* standard of mass formulae, the finite-range liquid drop model (FRDM) [3], when phenomenological corrections are added for certain correlation effects. Namely, a rotational energy correction is added when the mean field state breaks spherical symmetry, and a Wigner term is added to account for the stronger neutron-proton correlation in nuclei having nearly equal numbers of neutrons and protons [4, 5]. The quality of the fits, either FRDM or mean-field + corrections, is in the range of 0.6–0.7 MeV rms.

Some time ago, Bohigas and Leboeuf [6] opened a discussion on limits of accuracy of theories of the nuclear masses by arguing that chaotic contributions to the nuclear wave function will ultimately limit the accuracy of any mean-field approach. Their rough estimate for this limit is a rms deviation of  $\sigma_{\text{rms}} \approx 500$  keV (see Eq. (26) for its definition), which is only slightly below the values achieved in the FRDM and the mean-field + corrections. On the other hand, applying noise analysis to available mass theories of various types, Barea *et al.* argue in Ref. [7] that the upper limit of mass predictability should be well below 100 keV. They find that global mass theories such as the FRDM or the HFB show correlated errors. Only the much better performing local mass models, as for example the Garvey-Kelson (GK) mass formulae [8, 9, 10] with a  $\sigma_{\text{rms}}$  as low as 86 keV, have residual errors which are consistent with white noise. Another interesting recent analysis was made by Molinari and Weidenmüller [11], who computed the effect on the ground state energy of the fluctuations associated with the coupling to states at tens of MeV of excitation. The estimate

in their Fig. 1 is about 100 keV, again much smaller than the accuracy achieved by the global mass fits. Summarizing the current status of the discussion about the limits of mass theories, it is likely that the current limit of about 600 keV is “not a physical phenomenon, but rather a characteristic arising from the mean-field approximation”, to quote the conclusion of Ref. [12].

Even the limit of 600 keV may be optimistic. Indeed, stripping away all phenomenological corrections, it was found in Ref. [13] that SCMF theories based on Skyrme parameterizations only achieve a factor of two improvement over the liquid drop model, yielding rms residuals in the range 1.5-1.7 MeV. The need for explicit treatment of correlations should not be surprising. A remarkable fact about nuclear structure physics is that the mean field approach works as well as it does, given the strong short-range character of the nucleon-nucleon interaction. In this respect, the nuclear problem is much more difficult than the problem of structure and binding of electronic systems. There, the interaction is smooth and the self-consistent field is a very good starting point. What saves the theory for nuclear systems is the fact that the correlations induced by the interaction largely have a short range themselves. This makes it plausible that they can be subsumed in an effective interaction. But not all correlation effects can be included by a renormalization of a short-range interaction. The electronic problem provides a nice example of this. In the usual Kohn-Sham theory, the energy functional is local or nearly local except for the kinetic energy and electrostatic interactions. This is quite inadequate to describe the long-range van der Waals interaction, which is absent in the mean-field wave function and thus a pure correlation effect.

Another way that long-range correlations come about is when a symmetry is broken in the mean field and in the corresponding density matrix. In the nuclear many-body problem, translational symmetry is always broken and rotational symmetry may or may not be broken depending on the nucleus. The true ground state of course has the symmetry restored, and the additions to the wave function that bring about the symmetry restoration are correlation effects that are necessarily long-range when the symmetry is a global one. From the point of view of making a theory of the masses, there are two important questions. The first is how large are the correlation energies associated with broken symmetries. Unless their size is greater than the target accuracy of theory, they can be ignored. In fact, both the center-of-mass energy and the rotational energy are large compared to the 600 keV present-day standard. The second question is how much the energy fluctuates from nucleus to nucleus. If the correlation energy varies very smoothly, it could remain unnoticed in a theory based on a fitted energy functional. This seems to be the case for the center-of-mass energy. While its size can be of the order of 10 MeV for the lighter nuclei, its fluctuations are much less important than those of the quadrupolar degrees of freedom (see [14]).

The situation is more precarious for the rotational energy. It fluctuates considerably from nucleus to nucleus, vanishing for spherical nuclei and having a magnitude of the order of several MeV for deformed nuclei. This provides a motivation to calculate this correlation energy explicitly rather than keeping it buried as part of the mean-field energy functional. However, it is dubious to treat it as a discrete quantity, present in some nuclei but not in others. The shape can fluctuate and the binary classification of spherical or deformed nuclei should be replaced by a continuum starting from rigid spherical, through soft transitional to statically deformed nuclei. Thus, one is led to seek a theory of the correlation energy that would include the energy associated with zero-point shape fluctuations as well as static deformations.

There are two leading candidates for a systematic and practical theory of long-range correlations effects taking mean field theory as the starting point. These are the RPA, generalized to QRPA in the presence of pairing, and the generator coordinate method (GCM). The RPA has an impeccable pedigree in quantum many-body theory, solving a long-range divergence problem in the calculation of the correlation energy for Coulomb interactions. However, balancing this are a number of drawbacks which we list:

- RPA does not converge well when the interactions are short ranged [15]. This becomes obvious when one notes that second-order perturbation theory for a contact interaction diverges, and that the usual formula for the RPA correlation energy incorporates the second-order perturbation.
- As a small-amplitude approximation, QRPA cannot be expected to give a good description of the correlated ground state in soft transitional nuclei and nuclei with coexisting minima, where the ground-state is spread over a wide range of deformations.

None of these problems of RPA are necessarily insurmountable. Concerning the convergence, one might explicitly exclude the second-order perturbation term to eliminate the divergence. Alternatively, one could regularize the interaction in some way. Along these lines, the authors of Ref. [16] calculated RPA correlation energies in the Sn isotope chain using nuclear field theory, a theory that replaces the microscopic particle-hole interaction with a surface-peaked multipole interaction. The criticism of RPA that it is limited to small amplitudes is not entirely justified in practice: it can treat the correlation energy associated with symmetry restorations which are large amplitude effects [18], although the quality of this approximate symmetry restoration is not always very good [17].

The other leading contender for a theory of correlation effects is the GCM, which we favor and apply in this work. The essential idea is that one considers a manifold of mean-field states in an external field, different

strengths of the external field generating different states. The important point is that the space is essentially determined by the functional form of the external field. Once the field or the set of fields is specified, the theory is completely systematic and applicable to all nuclei for which the mean field is a reasonable starting point. The GCM is a “horizontal” extended theory in that the added parts to the wave function are low energy configurations, because they were obtained by the mean-field minimization procedure. This contrasts to the RPA approach, which invokes a “vertical” extension of the wave function to arbitrary high energy, but to only states that can be accessed by a one-body operator. Since we mentioned a number of drawbacks of (Q)RPA, we also make a similar list for the GCM. Namely:

- Convergence can be an issue on a numerical level. The theory is usually couched in terms of a continuum of mean-field states, but in practice computations are carried out with finite sets of states. If there are too many states in the basis of non-orthogonal states, they will be redundant and the matrix techniques to find the lowest energy state become unstable.
- For numerical reasons, we are limited at present to a single external field. We take it to be the isoscalar axial quadrupole field,

$$Q_2 = 2z^2 - x^2 - y^2 \quad (1)$$

leaving out higher multipoles and non-axial quadrupolar deformations.

- Already for  $J = 2$  excitations, it may be insufficient to take only the single generating field from Eqn. (1). This suspicion is raised by systematic overestimations of quadrupole excitations in rigid spherical nuclei [19, 20].

In the present paper we aim at a systematic study of the quadrupole correlation energy for all even-even nuclei where the mass is known. The quadrupole correlation can be expected to be the dominant correlation mode for all but doubly magic nuclei, so this is at least a reasonable first step to a complete theory. Starting from a self-consistent mean-field model based on Skyrme’s interaction, we restore particle-number and rotational symmetry and perform a configuration mixing of states with different quadrupole moment. Our approach does not aim at a nuclear mass formula, but has the long-range goal of a universal nuclear model that allows for the simultaneous consistent and systematic description of many observables, including excited states, for all nuclei. Such a strategy has obvious advantages for the most prominent application of nuclear mass formula, the description of nucleosynthesis in astrophysics. For example, the dynamics of the  $r$  process of explosive nucleosynthesis is determined by many nuclear properties [21, 22], with masses being just the simplest one.

The paper is organized as follows: In section II, we present the equations to be solved and discuss some technical aspects. In Section III, the physics of quadrupole correlations is discussed on a few typical examples. A systematic calculation for the correlation energies of 605 even-even nuclei is presented in section IV while in Sect. V, we analyze the effect of correlation energies on mass residuals. In section VI we discuss the role of quadrupole correlation energies from the point of view of mass models. In Sect. VII, we examine the role of quadrupole correlations for charge radii. A summary and our conclusions are presented in Sect. VIII. Some of the key results for quadrupole correlation energies have been presented earlier in a letter [23].

## II. CALCULATIONAL PROCEDURE

### A. Mean Field

We start with a set of self-consistent solutions of the HF+BCS generated with the code **ev8** [24, 25]. The single-particle wave functions are discretized on a three-dimensional Lagrange mesh [26] corresponding to a cubic box. The only restriction of the wave function is that the Slater determinant of the orbits is invariant with respect to parity, time reversal, and axial rotations. As in earlier studies, we use a fixed mesh spacing of 0.8 fm. The length of the box side ranges from 25.6 to 28.8 fm with the nucleus at the center. To avoid the breakdown of pairing correlations for small level densities around the Fermi surface, we perform an approximate projection-before-variation on particle number within the Lipkin-Nogami (LN) scheme as outlined in [27]. States with different mass quadrupole moments are generated by adding a constraint to the mean-field equations to force the quadrupole moment, Eqn. (1), to have some value

$$q = \langle Q_2 \rangle. \quad (2)$$

Higher even axial multipole moments are automatically optimized for a given mass quadrupole moment. For numerical stability of the constrained mean-field equations in light nuclei, the constraint is damped at large distances from the nuclear surface with the method proposed by Rutz *et al.* in Ref. [28].

The Skyrme interaction SLy4 [29] is used for the energy-density functional in the particle-hole channel. Pairing effects are treated in the BCS approximation using a density-dependent zero-range force, truncated above and below the Fermi surface as described in Ref. [30]. As in earlier studies, the pairing strength is taken to be  $-1000$  MeV fm $^3$  for both protons and neutrons.

While the wave functions are constructed using the code **ev8**, all energies and matrix elements are calculated with another code, **promesse** [31], which uses a more accurate algorithm for the kinetic energy. For SCMF

energies, this code has an accuracy for a mesh size of 0.8 fm given roughly by  $0.007 A$  MeV, where  $A$  is the mass number. This error varies quite smoothly with  $A$ . For even better accuracy, the mesh spacing should be decreased. Highly accurate SCMF calculations are also achieved using a deformed harmonic oscillator basis; see Ref. [32] for code details.

## B. Beyond the Mean Field

The application of the generator coordinate method that we do here goes beyond mean field in three respects: projections on good particle numbers, projection on angular momentum  $J = 0$ , and mixing deformations. Projection is a special case of the GCM, where the collective path and the weight functions are determined by the restored symmetry. Angular-momentum projection mixes states with all the possible orientations of the quadrupole tensor and therefore generates part of the quadrupole correlations. For this reason, to introduce consistently quadrupole correlations, the mixing of states with respect to the quadrupole moment by the GCM should be performed together with an angular-momentum projection.

Eigenstates of the particle-number operator  $\hat{N}$  with an even eigenvalue  $N_0$  are obtained by applying the particle-number projection operator

$$\hat{P}_N(N_0) = \frac{1}{\pi} \int_0^\pi d\phi_N e^{i\phi_N(\hat{N}-N_0)}, \quad (3)$$

separately for protons and neutrons. All the results presented in this paper include particle-number projection and we drop the indices  $N_0$  and  $Z_0$  to simplify the notations. To avoid the use of the Lipkin-Nogami correction of mean-field energies which is known to be often inaccurate, the mean-field energies corresponding to the Skyrme and pairing interactions have been recalculated by projecting the SCMF states on particle number. Thus, in the following, what we call SCMF energy is in fact the energy corresponding to a particle-number projected SCMF state. This projection is always performed on mean-field states which have  $N_0$  and  $Z_0$  as average particle numbers.

Formally, eigenstates  $|JMq\rangle$  of the angular momentum operators  $\hat{J}^2$  and  $\hat{J}_z$  with eigenvalues  $J(J+1)$  and  $M$  are obtained by applying the operator

$$\hat{P}_{MK}^J = \frac{2J+1}{16\pi^2} \int_0^{4\pi} d\alpha \int_0^\pi d\theta \sin(\theta) \int_0^{2\pi} d\gamma \mathcal{D}_{MK}^{*J} \hat{R}, \quad (4)$$

on the states  $|q\rangle$ . The rotation operator  $\hat{R}$  and the Wigner function  $\mathcal{D}_{MK}^J$  both depend on the Euler angles  $\alpha, \theta, \gamma$ . In practice, we shall simplify the 3-dimensional integral over Euler angles to a one-dimensional integral (see Eqns. (8-9) below).

The second step in treating quadrupole correlations is to mix configurations of different deformations. The mixed projected many-body state is set up as a coherent

superposition of normalized projected mean-field states  $|JMq\rangle$  with different intrinsic deformations  $q$

$$|JMk\rangle = \sum_q f_{Jk}(q) |JMq\rangle. \quad (5)$$

The weight function  $f_{J,k}(q)$  is determined to minimize the energy expression

$$E_k = \frac{\langle JMk|\hat{H}|JMk\rangle}{\langle JMk|JMk\rangle}. \quad (6)$$

where we have omitted the angular momentum indices on  $E_k$  since we will only be interested in the following to  $J = 0$  states. The solution is given by a matrix eigenvalue equation that corresponds to the discretized Hill-Wheeler-Griffin (HWG) equation [33, 34]

$$\sum_{q'} [H_J(q, q') - E_k I_J(q, q')] f_{J,k}(q') = 0. \quad (7)$$

For each  $J$ -value, the HWG equation gives a full spectrum of correlated states corresponding to the collective variable  $q$ . This spectrum can be used to study collective excitations, see, e.g., [35, 36] and references given therein. Here we are only interested in the  $J = 0$  ground state. Note that the exact number projection avoids some problems that may arise in calculating HWG matrix elements with BCS wave functions [35].

The angular momentum projection simplifies to a one-dimensional integral when the mean-field states are axial and time-reversal invariant. We take the  $z$  axis as a symmetry axis and the mean-field states as eigenstates of the  $z$  projection of the angular momentum in the intrinsic frame, with eigenvalue  $K = 0$ . The study of only even-even nuclei permits us to use a reduced interval for the angular integration. The angular-momentum projected norm and Hamiltonian kernels entering Eqn. (7) are then given by

$$\begin{aligned} I_J(q, q') &= \langle JMq|JMq'\rangle \\ &= \frac{1}{\mathcal{N}_J(q)\mathcal{N}_J(q')} \int_0^{\pi/2} d\theta \sin(\theta) d_{00}^J(\theta) \langle q|\hat{R}(\theta)|q'\rangle \end{aligned} \quad (8)$$

$$\begin{aligned} H_J(q, q') &= \langle JMq|\hat{H}|JMq'\rangle \\ &= \frac{1}{\mathcal{N}_J(q)\mathcal{N}_J(q')} \int_0^{\pi/2} d\theta \sin(\theta) d_{00}^J(\theta) \langle q|\hat{R}(\theta)\hat{H}|q'\rangle. \end{aligned} \quad (9)$$

with

$$\mathcal{N}_J(q) = \sqrt{\int_0^{\pi/2} d\theta \sin(\theta) d_{00}^J(\theta) \langle q|\hat{R}(\theta)|q'\rangle}. \quad (10)$$

The description of odd and odd-odd nuclei would require to break time reversal and axial symmetries [37], increasing the complexity of the calculation by several orders of magnitude.

Note that the weight functions  $f_{J,k}(q)$  in Eqn. (5) are not orthogonal. A set of orthonormal collective wave functions  $g_{Jk}(q)$  in the basis of the intrinsic states is obtained by a transformation involving the square root of the norm kernel [1, 18].

The expressions given above are written for a many-body Hamiltonian,  $\hat{H}$ . In practice, however, we use an energy density functional for the effective interaction, replacing all densities in the functional are by their corresponding transition densities.

In terms of the computational algorithms, an important technical challenge of a configuration-mixing calculation is the computation of the non-diagonal matrix elements between mean-field states. These are evaluated with the help of a generalized Wick theorem [38]. The single-particle states are discretized on a 3-dimensional mesh in coordinate space using a Lagrange mesh technique [26]. Thanks to the imaginary time step method [39], only a small fraction of the single-particle states which could be constructed on the mesh need to be computed. As a result, the two sets of single-particle states corresponding to two mean-field solutions are not equivalent, which has to be carefully taken into account [40, 41]. The overlaps are calculated with the Onishi formula. It contains a square root evaluation, which has a sign ambiguity that requires some additional care.

Another technical problem that appears at the level of solving the HWG equation (7) is the possible over-completeness of the basis states  $|q\rangle$ . This can lead to problems of numerical stability, see Sect. II F below.

### C. Definition of correlation energies

The energy of an angular-momentum projected mean-field state of deformation  $q$  is given by the diagonal matrix elements of the Hamiltonian kernel (9)

$$E_0(q) = H_0(q, q). \quad (11)$$

We denote the energy of a SCMF state  $|q\rangle$  as  $E(q)$ . The energy gained by the projection of a state  $|q\rangle$  is its *rotational energy*

$$E_{\text{rot}}(q) = E(q) - E_0(q). \quad (12)$$

This energy can be computed in approximate ways without getting into the details of a full projection [35].

Starting from the SCMF energy landscape  $E(q)$ , several correlation energies can be defined. The static *deformation energy* is the energy difference between a mean-field configuration  $q$  and the spherical one

$$E_{\text{def}}(q) = E(Q_2 = 0) - E(q). \quad (13)$$

The minimum of  $E(q)$  is the SCMF energy,  $E_{\text{mf}}$ , and corresponds to a deformation  $q_{\text{mf}}$ .

After angular momentum projection, the minimum of  $E_0(q)$  may correspond to a different configuration  $q$  that

we label  $q_0$ . It is more useful to define correlation energies which can be simply added to the SCMF energy binding energy. For angular-momentum projection, we introduce the *rotational energy correction*:

$$\begin{aligned} E_{J=0} &= E(q_{\text{mf}}) - E_0(q_0) \\ &= [E(q_{\text{mf}}) - E(q_0)] + E_{\text{rot}}(q_0), \end{aligned} \quad (14)$$

in which the first term represents a loss of energy due to mean-field deformation and the second (larger) term the gain due to angular momentum projection.

The correlation energy gained by configuration mixing is then defined with respect to  $E_{J=0}$ :

$$E_{\text{GCM}} = E_0(q_0) - E_{k=0}. \quad (15)$$

Both  $E_{J=0}$  and  $E_{\text{GCM}}$  are non-negative since they are determined by a variational calculation. As a consequence, the nucleus is always more bound by correlations.  $E_{J=0}$  is also non-negative in other more approximate treatments of projection. However, when treating configuration mixing through a Bohr Hamiltonian or a collective Schrödinger equation, the potential energy surface has a different meaning. It contains a (local) vibrational term (strangely named "zero point energy correction") which has the same sign as  $E_{\text{GCM}}$ . It is also used as a collective potential in which vibrational states are calculated, adding a second contribution to  $E_{\text{GCM}}$  of the opposite (negative) sign.

The total *dynamical correlation energy* is given by the energy difference between the mean-field ground state and the projected GCM ground state

$$\begin{aligned} E_{\text{corr}} &= E(q_{\text{mf}}) - E_{k=0} \\ &= E_{J=0} + E_{\text{GCM}}. \end{aligned} \quad (16)$$

Our separation of the dynamical quadrupole correlation energy  $E_{\text{corr}}$  into a rotational and a vibrational part is somewhat arbitrary. An alternative choice would be to define the rotational correlation energy as the rotational energy of the mean-field ground state  $E_{\text{rot}}(q_{\text{mf}})$ , and take as vibrational energy the energy gained by the GCM with respect to  $E_{\text{rot}}(q_{\text{mf}})$ . Such a choice would lead to smaller rotational but larger vibrational energies, but leaves  $E_{\text{corr}}$  of course invariant. We prefer the separation we have chosen through Eqns. (14) and (15), that we find easier to interpret.

### D. Two-point topGOA for angular-momentum projection

The elementary operations of our calculation are the computation of the overlap  $\langle q|\hat{R}(\theta)|q'\rangle$  and the Hamiltonian  $\langle q|\hat{R}(\theta)\hat{H}|q'\rangle$  matrix elements between two mean-field wave functions corresponding to different quadrupole moments and to different orientations in space. For a large-scale calculation as performed here,

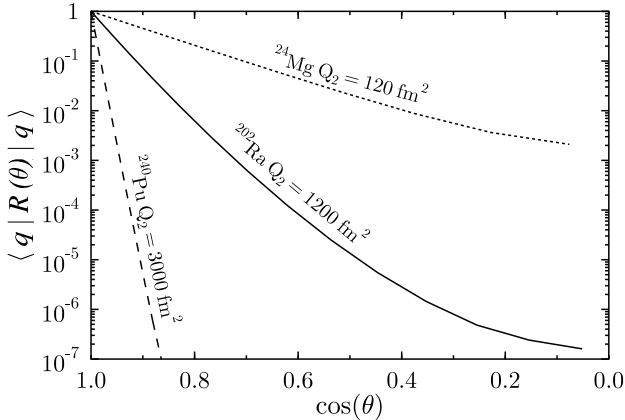


FIG. 1: Overlap  $\langle q|\hat{R}(\theta)|q\rangle$  as a function of  $\cos(\theta)$  for a state close to the projected minimum in  $^{24}\text{Mg}$ ,  $^{202}\text{Ra}$ , and  $^{240}\text{Pu}$ .

it is compulsory to devise an efficient algorithm to reduce the number of these elementary steps. This can be done at two places. First, the number of discrete angles  $\theta$  necessary to evaluate the kernels in Eqns. (8) and (9) can be reduced using a topological Gaussian overlap approximation (topGOA) [42, 43] for the  $\theta$  dependence of  $\langle q|\hat{R}(\theta)|q'\rangle$  and  $\langle q|\hat{R}(\theta)\hat{H}|q'\rangle$ . Next, the number of matrix elements to be calculated as a function of  $q$  can be reduced by a second GOA, this time for non-diagonal angular-momentum projected matrix elements between states with different quadrupole moment.

It has to be stressed that the GOA method as we use it is only a numerical tool and is quite different from the formal approximations based on the GOA which are often used in the literature [40, 44, 45, 46, 47, 48, 49]. In the framework of this approach, the GOA constitutes the first step to derive a collective Schrödinger equation or a microscopic Bohr-Hamiltonian. By expanding the overlap and energy kernels around the diagonal matrix elements and assuming a Gaussian shape in an appropriate set of coordinates, local collective mass parameters and potentials are derived and used to construct a collective equation. By contrast, we still solve the projected HWG equation, Eqn. (7) in our method. Selected matrix elements are computed to high precision, allowing us to construct a reliable approximation of the full GCM kernels.

A first study of the feasibility of this approach was presented in Ref. [43]. In the course of the large-scale calculations reported below, we found that the GOA scheme has to be slightly modified to ensure convergence of the method in specific nuclei, mostly light ones and some transitional heavy ones near magic numbers.

With the exception of the cases specified below, an adequate approximation to the norm and Hamiltonian kernels as a function of  $\theta$  is given by a two-point approximation

$$\begin{aligned} \langle q|\hat{R}(\theta)|q'\rangle &= \langle q|q'\rangle e^{-c_2(q,q')\sin^2(\theta)} \\ \langle q|\hat{R}(\theta)\hat{H}|q'\rangle &= \langle q|q'\rangle e^{-c_2(q,q')\sin^2(\theta)} \end{aligned} \quad (17)$$

$$\times [h_0(q, q') - h_2(q, q') \sin^2(\theta)], \quad (18)$$

where  $\langle q|q'\rangle$  is the overlap between unrotated states and  $h_0(q, q')$  the Hamiltonian kernel between unrotated states. The width of the Gaussian and the expansion coefficient in the Hamiltonian kernel are determined from the matrix element where the left state is rotated by the angle  $\theta_2$

$$c_2(q, q') = \langle q|\hat{R}(\theta_2)|q'\rangle \quad (19)$$

$$h_2(q, q') = \langle q|\hat{R}(\theta_2)\hat{H}|q'\rangle. \quad (20)$$

A thorough discussion of this particular choice for the GOA and examples for the quality of this approximation can be found in Ref. [43].

The angle  $\theta_2$  has to be chosen large enough to be sensitive to the variation of the overlap but small enough to fit the integrand in the region where it brings a large contribution. Fig. 1 shows typical overlap functions for different nuclei. For magic nuclei and small deformations, the overlaps do not decrease strongly with  $\theta$  while for  $^{240}\text{Pu}$ , at the ground state deformation, it falls by two orders of magnitude at a rotation angle of  $15^\circ$ . Obviously the appropriate choice of  $\theta_2$  depends on the nucleus. We determine it from the properties of the mean-field solution, making use of the approximate overlap function derived by Baye and Heenen in Ref. [50]. It reduces in our case of axial nuclei to:

$$\langle q|\hat{R}(\theta)|q\rangle \approx \exp \left\{ -[1 - \cos(\theta)] \langle \hat{J}_\perp^2 \rangle \right\}, \quad (21)$$

where  $\langle \hat{J}_\perp^2 \rangle$  is the dispersion of the angular momentum perpendicular to the symmetry axis of the mean-field state  $|q\rangle$ . We choose  $\theta_2$  to give an overlap of  $1/2$  according to Eqn. (21). However, if the equation has no solution, we set  $\cos(\theta_2) = 1/\sqrt{2}$ . The estimate in Eqn. (21) requires that the left and right states be the same. For matrix elements between different states – and therefore different  $\langle \hat{J}_\perp^2 \rangle$  – we use the  $\langle \hat{J}_\perp^2 \rangle$  that is larger.

Matrix elements between oblate and prolate deformations require special treatment [43] because their overlaps peak at  $\theta = \pi/2$  rather than  $\theta = 0$ . These matrix elements are calculated with a three-point approximation described below.

### E. Three-point topGOA for angular-momentum projection

For about 10 % of the nuclei included in this study, often when the overlap varies slowly with the rotation angle, a two-point topGOA approximation is not accurate enough, and a higher-order approximation has to be used. We found a three-point approximation sufficient in these cases. In the three-point topGOA, the overlap and Hamiltonian kernels are approximated by

$$\langle q | \hat{R}(\theta) | q' \rangle = \langle q | q' \rangle e^{-c_2(q, q') \sin^2(\theta) - c_4(q, q') \sin^4(\theta)} \quad (22)$$

$$\langle q | \hat{R}(\theta) \hat{H} | q' \rangle = \langle q | q' \rangle e^{-c_2(q, q') \sin^2(\theta) - c_4(q, q') \sin^4(\theta)} [h_0(q, q') - h_2(q, q') \sin^2(\theta) - h_4(q, q') \sin^4(\theta)]. \quad (23)$$

The additional parameters  $c_4, h_4$  are obtained by demanding exact values for the angles  $\theta = 0, \theta_2$ , and  $\theta_3 = \pi/2$ .

In Fig. 2, the overlap and energy functions calculated with the two-point and three-point topGOA are compared with the exact ones. The example chosen is a case for which the two-point approximation is inadequate, the diagonal matrix element at  $Q_2 = 200 \text{ fm}^2$  in the nucleus  $^{104}\text{Te}$ . The rotation angles used for the topGOA are shown as dots. The two-point approximation clearly underestimates the overlap at large angles, which leads to too small a projected overlap. The three-point topGOA, on the other hand, cannot be distinguished from the exact calculation within the resolution of the plot. The Hamiltonian matrix element is also underestimated at large angles, by an even greater amount. This is shown in the right panel of Fig. 2. One also sees that three-point approximation has only a small difference from the exact

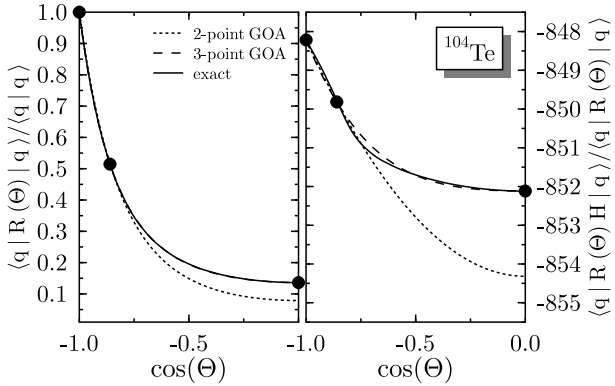


FIG. 2: Comparison between two-point (dotted line) and three-point GOA (dashed line) and an exact projection (solid line) for the diagonal overlap (left panel) and energy (right panel) matrix elements for  $^{104}\text{Te}$  at a deformation  $Q_2 = 200 \text{ fm}^2$ . A normalization factor  $1/\langle q | \hat{R}(\theta) | q \rangle$  is included in the energy that does not enter the calculation of the Hamiltonian kernel. All matrix elements are projected on particle number  $N = Z = 52$ .

TABLE I: Comparison between different levels of approximation for the  $J = 0$  norm and energy of the  $Q_2 = 200 \text{ fm}^2$  mean-field state of  $^{104}\text{Te}$ .

method	$\langle q   \hat{P}_{00}^0   q \rangle$	$\langle q   \hat{P}_{00}^0 \hat{H}   q \rangle / \langle q   \hat{P}_{00}^0   q \rangle$
two-point topGOA	0.0618	-850.753
three-point topGOA	0.0705	-850.487
full projection	0.0706	-850.488

function.

The values obtained for the projection on  $J = 0$  of the overlap and the energy are given in Table I. As expected, the overlap and the energy obtained with a two-point topGOA approximation are significantly too small, while the three-point approximation agrees perfectly with the exact result.

The three-point GOA has been used for nuclei with less than 22 neutrons or protons and for configurations with very small prolate or oblate deformations. The most critical heavy nuclei differ from magic numbers by two nucleons or by an  $\alpha$  particle. All other matrix elements were calculated as described in Ref. [43].

## F. Mixing deformations

The next step in treating correlations by the GCM is to select a set of deformed configurations, compute the required matrix elements in Eqn. (7), and diagonalize the corresponding eigenvalue problem.

Given a set of  $n_c$  configurations, the number of overlap or Hamiltonian computations needed to generate a matrix for Eqn. (7) is  $n_c(n_c+1)/2$ . As explained in Ref. [43], the effort can be drastically reduced, to linear order in  $n_c$ , by using a topological GOA in the deformation coordinate. In the simple case, this requires only calculation of diagonal and nearest-neighbor off-diagonal matrix elements, i.e.  $2n_c - 1$  elements per matrix. A subtlety that arises is that  $Q_2 = 0$  is a singular point for the GOA. This does not cause any difficulty if the nucleus is well deformed either prolate or oblate, but must be dealt with if the ground state wave function has significant mixing between prolate and oblate deformations. We drop the  $Q_2 = 0$  configuration which is nearly redundant with our configuration spaces. We believe that the correlation energies have a numerical accuracy of about 200 keV with respect to a fully converged GCM.

Some typical configuration sets for heavy nuclei are shown in Table II. The table enumerates the configurations used for the GCM in those nuclei. The points are not equidistant, but selected in such a manner that they resolve the structures in the  $J = 0$  potential energy curve, and asking that the overlaps between neighboring configurations are above 0.5 and, if possible, below 0.7. According to Ref. [40], this range is sufficient to produce final energies having errors of less than 200 keV. In some cases, however, we have to add points with larger overlap to ensure that we represent all structures in the potential landscape. For spherical nuclei the selection of points requires some search by trial and error. A set

TABLE II: Configuration spaces for typical heavy nuclei. Mass quadrupole moments  $q$  are given in barns. Oblate and prolate configurations are listed on separate lines.

nucleus	$n_c$	$q$ values
$^{208}\text{Pb}$	12	-20 -15 -10 -7.5 -5 -2.5 +2.5 +5 +7.5 +10 +15 +20
$^{180}\text{Hg}$	17	-24 -20 -16 -14 -10 -6 -4 +4 +6 +8 +12 +16 +20 +24 +28 +32 +36
$^{170}\text{Hf}$	14	-24 -20 -16 -13.75 -10 -5 +5 +10 +15 +19.25 +22 +25 +30 +35

of deformations that can be used for a nucleus with a given structure, however, works usually also for adjacent ones of the same type. We usually include a few more points than necessary to obtain convergence of the GCM ground-state energy.

Numerical stability of the eigenvalue problem is also an issue in these computations. For a given set of deformations, we always diagonalize the overlap matrix first, and then remove by trial and error the states with lowest norm eigenvalues until we obtain a stable solution of the HWG equation that is not contaminated by spurious states. In some cases the selection of deformations has to be modified to remove spurious states.

#### G. Assessment of the numerics

Thanks to the use of the numerical approximations listed in the previous section, a huge factor in computing time is gained without significant loss of accuracy. Projection on angular momentum requires  $n_j$  Euler angles (5 to 15) and the GCM mixing in quadrupole moment  $n_c$  deformed states (7 to 25). This gives  $n_j \times n_c(n_c+1)/2 \approx 150\text{-}5000$  matrix element evaluations altogether. Our numerical GOA saves a factor of 2 to 3 on  $n_j$  as well as a much larger factor on completing the Hill-Wheeler matrices. We end up having about  $n_j \times [n_c + (n_c-1)] \approx 26\text{-}100$  matrix elements only to calculate exactly. The GOA as we have done it is designed to describe accurately the correlations in the  $0^+$  ground state and most information for spectroscopy is lost. Note that particle-number projection is still performed exactly. Our numerical procedure is tuned to achieve a total accuracy better than 300 keV. This is sufficient for a study of the systematics of quadrupole correlation energies, which are an order of magnitude larger.

### III. SELECTED EXAMPLES

Figure 3 shows the energy curves (top) and the collective wave functions (bottom) obtained for cases represen-

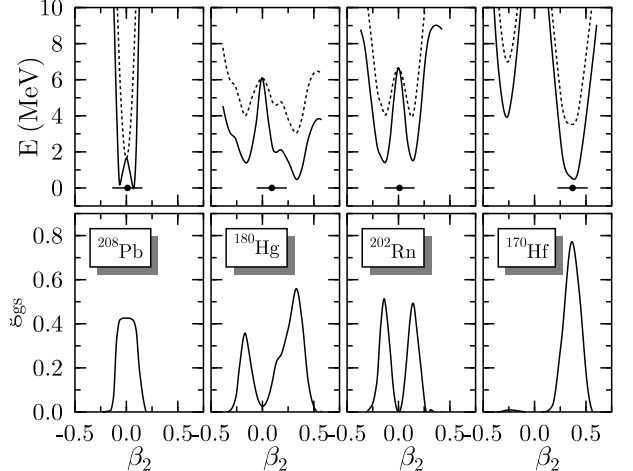


FIG. 3: Upper panel: Topology of unprojected/projected energy landscapes of typical heavy nuclei. The dotted line denotes the energy after projection on particle-number only, the solid line the energy after projection and particle-number and angular-momentum  $J = 0$ . The dot denotes the energy of the  $J = 0$  projected GCM ground state. Lower panel: Collective  $J = 0$  ground-state wave function. All curves and markers are drawn versus the average axial quadrupole deformation of the mean-field states they are constructed from.

tatives of the topographies that one encounters in heavy nuclei: spherical, soft and well deformed. The curves are plotted as a function of a dimensionless axial mass quadrupole deformation  $\beta_2$  defined by:

$$\beta_2 = \sqrt{\frac{5}{16\pi}} \frac{4\pi}{3R^2A} \langle \hat{Q}_2 \rangle \quad (24)$$

with  $R = 1.2 A^{1/3}$ . After angular-momentum projection, we still use the  $\beta_2$  value of the (unprojected) mean-field state to label the projected  $J = 0$  states, although all  $J = 0$  states have a zero quadrupole moment in the laboratory frame. The energy curves projected on  $J = 0$  are also shown in Fig. 3. Finally, a circle in the middle of a bar indicates the mean deformation of the GCM states, defined as:

$$\bar{\beta}_2 = \int d\beta_2 \beta_2 g_{J,k}(\beta_2). \quad (25)$$

The doubly-magic  $^{208}\text{Pb}$  exhibits a very stiff potential energy curve. Angular momentum projection on  $J = 0$  does not change that overall behavior, but shifts the minimum of the potential energy curve to a small, but finite, deformation, a common feature for all angular-momentum projected energy surfaces of spherical nuclei [35, 43]. A spherical mean-field state is already a  $J = 0$  state, and therefore not at all affected by projection. Projecting the  $J = 0$  component from a slightly deformed state, usually with  $|\beta_2|$  values below 0.1, often leads to a substantial energy gain, 1.7 MeV in the case of  $^{208}\text{Pb}$ . Imposing axial symmetry, as done here, the projection generates two

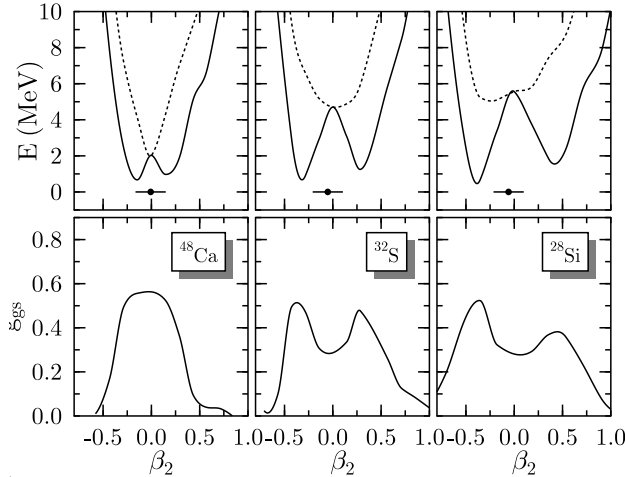


FIG. 4: The same as 3, but for light nuclei.

minima which are nearly degenerate and have similar deformation. The overlaps  $\langle Jq|J-q \rangle$  between these minima are very close to one: 0.91 in the case of  $^{208}\text{Pb}$ . These large overlaps show the limits of labelling projected states by  $\beta_2$ : the  $J = 0$  states obtained by projecting slightly oblate and prolate configurations are nearly identical. They have the same weight in the GCM ground state of a spherical nucleus. One of them is, in principle, redundant, a familiar feature when working in a basis of non-orthogonal states. The energy gain from the mixing of different deformations is very small, around 100 keV.

$^{180}\text{Hg}$  is an example of a transitional nucleus showing shape coexistence. The mean-field curve presents two minima, prolate and oblate, the corresponding wave functions having a very small overlap, of the order of  $10^{-5}$ . The energy gain by angular momentum projection is somewhat larger than in  $^{208}\text{Pb}$ , but the overall shape of the potential landscape is not altered by angular-momentum projection. There is also a large spreading of the collective ground state wave function which, in particular, mixes prolate and oblate shapes. The energy gain from the configuration mixing is relatively small, 0.5 MeV only.

$^{170}\text{Hf}$  is a well-deformed nucleus from the upper end of the rare-earth region. The mean-field energy curve presents a deep prolate minimum, the static deformation of the nucleus bringing an energy gain of 12.2 MeV. Projection of the mean-field energy curve on  $J = 0$  does not modify the deformation of the minimum but leads to a gain in binding energy of 2.9 MeV and the GCM mixing of shapes an extra 0.5 MeV.

The topography of the surface for  $^{202}\text{Rn}$  is intermediate between  $^{170}\text{Hf}$  and  $^{180}\text{Hg}$ , with two well defined mean-field oblate and prolate minima of moderate deformations which are still present after projection. The configuration mixing gives nearly equal weights to the oblate and prolate deformations, as can be seen on the collective wave function, the value of  $\bar{\beta}_2$  being close to zero.

TABLE III: Quadrupolar deformation and correlation energies in MeV of the nuclei in Figs. 3 and 4 (see text).

nucleus	$E_{\text{def}}$	$E_{J=0}$	$E_{\text{GCM}}$	$E_{\text{corr}}$
$^{208}\text{Pb}$	0.0	1.7	0.0	1.7
$^{180}\text{Hg}$	3.0	2.6	0.5	3.1
$^{170}\text{Hf}$	12.2	2.9	0.5	3.4
$^{202}\text{Rn}$	2.6	2.7	1.4	4.0
$^{48}\text{Ca}$	0.0	1.4	0.7	2.0
$^{32}\text{S}$	0.0	3.8	0.9	4.7
$^{28}\text{Si}$	0.7	4.2	0.6	4.9

The situation is different in light nuclei, as can be seen in Fig. 4. While magic nuclei like  $^{48}\text{Ca}$  remain stiff and gain only small amounts of dynamical correlation energy, the ground state of all light open-shell nuclei is dominated by dynamical correlations. As fewer single-particle states cross the Fermi level when deforming light nuclei, the likelihood to create significantly different mean-field configurations and coexisting minima is much lower. With our choice of mean-field and pairing interactions, there are even only very few light nuclei with a deformed mean-field ground state (see below). The energy gain from projection is larger than the static deformation energy, so all non-doubly-magic nuclei have very similar potential energy landscapes, in most cases with nearly degenerated prolate and oblate minima, that are strongly mixed by the GCM. Table III summarizes the energy gain at each step when going from a spherical mean-field state to the  $J = 0$  projected GCM state.

Some words of caution are necessary here about the vocabulary that we use to describe our results. Deformation is a well defined concept for a mean-field state and it can be quantified either by an intrinsic quadrupole moment or by the parameter  $\beta_2$  defined by Eqn. (24). After projection on angular momentum, a  $0^+$  state has of course a zero quadrupole moment in the laboratory frame. One can still relate each projected state to a specific mean-field configuration, and we use it to characterize the projected state. However, this relation has some limits. First, as very well illustrated by the case of  $^{208}\text{Pb}$ , the states obtained by projection of mean-field states with different deformations may have very large overlap, in particular when they are nearly spherical. Also, there is no implication that a weakly deformed configuration has a rotational band. For  $^{208}\text{Pb}$ , for example, the angular-momentum projected  $2^+$  state would correspond to a very different expansion of projected mean-field states and have a very different mean deformation  $\bar{\beta}_2$ . It is only for cases like the well-deformed nucleus  $^{170}\text{Hf}$  that one can expect very similar collective wave functions for different values of  $J$ . In particular, this is the only case where it makes sense to associate  $\bar{\beta}_2$  with the  $B(E2)$  values of the ground state band as, e.g., in the collective rotor model.

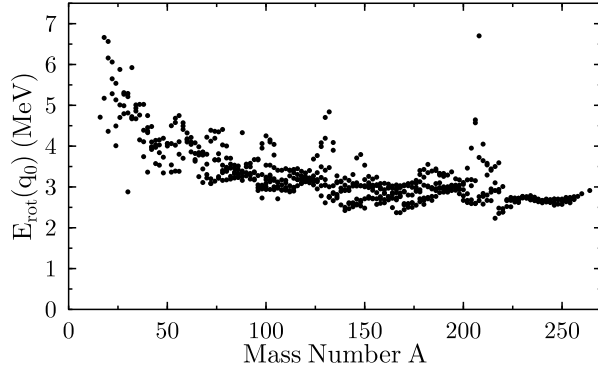


FIG. 5: Rotational energy  $E_{\text{rot}}(q_0)$  at the minimum of the  $J = 0$  projected energy curve.

#### IV. OVERVIEW OF CORRELATION ENERGIES

##### A. Angular momentum projection energies

The angular momentum projection energies  $E_{\text{rot}}(q_0)$  are plotted in Fig. 5 as a function of the mass number for the 605 nuclei that we have calculated. One sees that they vary rather smoothly, decreasing from about 6 MeV in light nuclei to 2.5 MeV for heavy ones. For a few nuclei around the doubly magic  $^{132}\text{Sn}$  and  $^{208}\text{Pb}$ ,  $E_{\text{rot}}(q_0)$  is much larger and deviate from the general trend. In particular, the value of  $E_{\text{rot}}(q_0)$  for  $^{208}\text{Pb}$  is about 7 MeV, but it is largely compensated by the loss of energy due to deformation. Taking this loss into account, one obtains the much smaller rotational energy correction  $E_{J=0}$  given in Table III.

These projection energies can be compared to values available in the literature. Egido, Robledo and Rodriguez-Guzman [35] also perform an exact projection on angular momentum of mean-field wave functions with an axial symmetry but with another effective interaction, the Gogny force [1] and without projection on particle number. Girod and coworkers [46] also use the Gogny force and have developed an approximation scheme for triaxial quadrupole deformations based on the GCM and leading to a collective Schrödinger equation. Their rotational correction is obtained from the Inglis-Belyaev moment of inertia [18] but also includes an *ad hoc* renormalization factor to take into account the Thouless-Valatin rearrangement contribution. Both Reinhard *et al.* [51] and Goriely *et al.* [60] use a Skyrme effective interaction. The approximation used by Reinhard *et al.* is similar to the one of Girod *et al.* and is derived from a local GOA approximation of projection. In the work of Goriely *et al.*, the rotational correction is determined with a moment of inertia calculated by a cranking formula, modified either by a rigid body term or, as in the most recent applications, rescaled at small deformations to behave in a realistic way.

A sample of results obtained with these different methods are shown in Table IV. The minima of the potential

TABLE IV: Angular momentum projection energies  $E_{\text{rot}}$  for selected cases compared with other calculations (see text).

Nucleus	$\beta_2$	This work	Other
$^{32}\text{Mg}$	-0.25	4.7	6.3 [51]; 4.0 [35]
$^{44}\text{S}$	-0.29	4.0	6 [51]
$^{98}\text{Zr}$	-0.11	3.3	3.8 [51]
$^{164}\text{Er}$	0.36	3.0	3 [35]
$^{198}\text{Hg}$	-0.15	3.3	3.1 [46]
$^{240}\text{Pu}$	0.30	2.7	3 [52]

energy landscapes determined in the five works quoted in Table IV might correspond to significantly different deformations since the effective interactions are not the same. We have therefore compared the values of the angular momentum projection energies for the deformation of the minimum that we have obtained here. One can indeed expect that this energy is not too sensitive to the details of the interaction and depends mainly on the geometry of the mean-field wave function which is projected. The values of the energies obtained by Egido, Robledo and Rodriguez-Guzman with an exact projection are rather close to our values. They also obtain very similar results for  $^{208}\text{Pb}$ , with a huge energy gain for a small deformation partly compensated by the loss of energy due to deformation. The projection energies obtained by Reinhard *et al.* are somewhat larger than ours; the values of Girod *et al.* which are determined from a very similar method are more similar but they include an *ad hoc* renormalization factor of 1.32 without which they would be closer to Reinhard's values than ours. The inclusion of a rigid body component in the calculations by Goriely *et al.* also seems important to obtain values close to those of an exact projection.

There are unfortunately not many values in the literature explicitly given for the correlation energies associated with configuration mixing. Reinhard *et al.* give vibrational energies for a sample of nuclei which should be an approximation of our correlation energies  $E_{\text{GCM}}$ . Both have indeed the same order of magnitude and also have the same effect of reducing the increase of deformation due to the rotational correction. Girod *et al.* treat these correlations as vibrations in a collective nuclear potential. This enables them to consider triaxial deformations at a low cost. However, the variational nature of the GCM is lost in their approximation and the corrections that they determine are zero-point energies which increase the energy of the (approximately) projected ground state.

##### B. Induced deformations

Without any exception, the mean-field configuration leading to the minimum of the projected energy curve is deformed. This is not surprising; the angular mo-

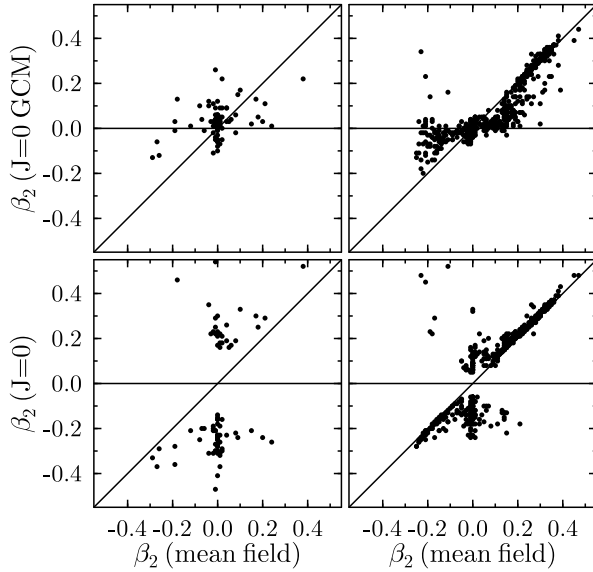


FIG. 6: Mean deformation of the GCM ground state for  $J = 0$  (top) and deformation of the mean-field configuration corresponding to the minimum of the  $J = 0$  energy curve (bottom). Both are plotted as a function of the deformation of the mean-field ground state. Left and right panels show light and heavy nuclei, respectively, divided at  $A = 60$ .

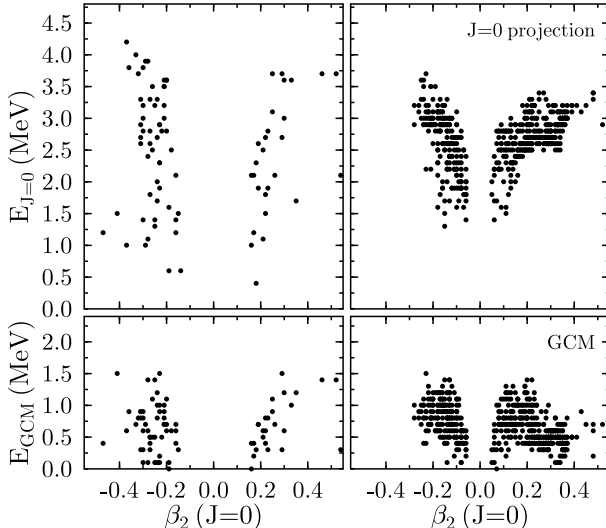


FIG. 7: Correlation energy  $E_{J=0}$  as a function of the deformation  $\beta_2(q_0)$  of the angular-momentum projected ground state. Left and right panels show light and heavy nuclei, respectively, divided at  $A = 60$ .

mentum projection of deformed intrinsic configurations permits the inclusion of small components in the wave function that might otherwise be treated as perturbative two-particle two-hole amplitudes [42]. In the bottom of Fig. 6 is plotted the deformation of the minimum of the  $J = 0$  energy curve as a function of the deformation of the mean-field ground state. Nuclei are divided into light (left) and heavy (right) ones. For heavy nuclei, both de-

formations are equal as soon as the deformation is of the order of 0.1, with a few exception corresponding to nuclei with a very soft surface or a deformed secondary minimum at low energy. For nuclei with masses lower than 60, both deformations are much more different, with the general tendency that projection increases the deformation. In the top panel of the same figure we plot the dependence of the mean deformation of the GCM state, as given by Eqn. (25), on the deformation of the mean-field ground state. Both quantities are quite close for heavy nuclei, even when the mean-field ground state is spherical. For light nuclei, the mean deformation of the projected GCM states are also closer to the deformation of the mean-field ground state than the deformation of the  $J = 0$  projected ground state, with, however, still large differences.

### C. Systematics of $E_{J=0}$ and $E_{\text{GCM}}$

Systematics of the correlation energies  $E_{J=0}$  and  $E_{\text{GCM}}$  are shown in Fig. 7 as a function of the deformation of the minimum of the angular-momentum projected energy curve.

Oblate and prolate configurations lead to correlation energies  $E_{J=0}$  of the same magnitude, with a large spreading as a function of  $\beta_2$ , smaller for heavy nuclei than for light ones. For deformations larger than  $\beta_2 = 0.2$ , these energies vary for heavy nuclei between 2.5 and 3.5 MeV and for light ones between 1.0 and 4.2 MeV.

The correlation energy associated with configuration mixing,  $E_{\text{GCM}}$ , is plotted in the lower panels of Fig. 7. It is smaller than  $E_{J=0}$  with a similar behavior for heavy and light nuclei. Although  $E_{\text{GCM}}$  could be close to zero for some nuclei, it can be as large as 1.5 MeV for others. There is no clear dependence of  $E_{\text{GCM}}$  on the magnitude or on the sign of  $\beta_2$ . Nuclei with small deformation  $\beta_2$  of the mean-field ground state may have correlation energies  $E_{\text{GCM}}$  as large as very deformed nuclei. It therefore does not seem possible to ascribe a dependence of  $E_{\text{GCM}}$  on the static  $\beta_2$  value. In collective models, the correlation energy comes from fluctuations in  $\beta_2$ . These can only be calculated by determining the curvature of the energy surface and the inertial parameter associated with that coordinate.

## V. MASS TABLE SYSTEMATICS

### A. SCMF energies

Before discussing the binding energy systematics we briefly describe the systematics of the residuals of binding energies at the SCMF level. Experimental masses are taken from Ref. [53]. On the lower panel of Figure 8 are shown the difference between SCMF energies and experiment, using the SLy4 functional and pairing defined in

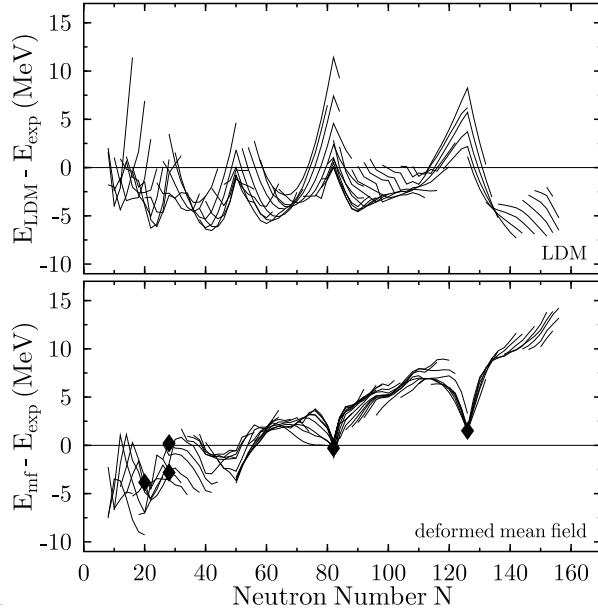


FIG. 8: Deviations between theoretical and experimental energies as a function of neutron number. The solid lines connect nuclei in isotopic chains. The liquid drop model, shown in the top panel, visibly under-binds magic nuclei near  $N = 50$ , 82 and 126. The bottom panel shows the SCMF for the SLy4 interaction, allowing axial deformations and including particle number projection. Markers denote the nuclei used in the fit of the SLy4 interaction. The numerical precision of the calculations about 1 MeV in heavy nuclei, with the error mostly proportional to  $A$ .

Section II A. The theoretical energies used for the figure include particle-number projection as well. Positive deviations denote under-bound nuclei. The plot of the corresponding residuals for the liquid drop model is shown on the upper panel. The residuals are obviously correlated in both approaches. One clearly sees the magic number effects, with the liquid-drop model under-binding magic nuclei, but the SCMF under-binding the nuclei in between. The residuals for the SCMF might appear large, but 5 MeV overbinding in light nuclei corresponds to a 3 % error on total energies, and 13 MeV under-binding out of nearly 2 GeV binding energy of a superheavy nucleus is an error of only 0.5 %. Still, applications of mass formulae to unknown nuclei require a much better precision.

The usual measure of the quality of a mass model is the rms residual energy, defined as

$$\sigma_{\text{rms}} = \sqrt{\frac{1}{N} \sum_{j=1}^N (E_j^{\text{exp}} - E_j^{\text{cal}})^2}. \quad (26)$$

The rms deviation  $\sigma_{\text{rms}}$  on masses for nuclei calculated in this study is 5.33 MeV, a value much larger than what can be achieved by recent HFB mass fits. Similar results have been obtained for SLy4 and other Skyrme interactions by Stoitsov *et al.* [54] using a slightly different treatment of pairing correlations. There are two distinct trends in the

deviations:

- There is a global trend with  $N$ , which tilts the median of the deviations. This overall wrong trend can be removed by a slight change in the parameters of SLy4, see Ref. [13] and Section VI below. It is probably an artifact of the fit protocol of the standard Skyrme interactions, which are adjusted solely to nuclear matter properties and to the binding energies and radii of a few magic nuclei. Such a global trend is not present in HFB mass fits [2, 4, 5, 55, 56, 57, 58, 59, 60] done on all known nuclear masses. It is also absent in the recent relativistic SCMF parameterization DD-ME2 by Lalazissis *et al.* [61].
- There are several local deviations. Some of them are obviously correlated to the spherical magic numbers: the closed-shell nuclei are over bound relative to the surrounding open-shell nuclei, which gives rise to characteristic “arches” between the shell closures. The same fluctuations appear in the relativistic SCMF of Ref. [61]. We will investigate if these local deviations are, totally or partially, related to dynamical quadrupole correlations beyond the mean field.

The diamonds in Fig. 8 mark the five double-magic nuclei ( $^{40}\text{Ca}$ ,  $^{48}\text{Ca}$ ,  $^{56}\text{Ni}$ ,  $^{132}\text{Sn}$ ,  $^{208}\text{Pb}$ ) whose binding energies were included in the fit of the SLy4 interaction. They all are close to the  $E_{\text{mf}} - E_{\text{exp}} = 0$  line, located either on the bottom of the ravines, or the top of the peaks ( $^{56}\text{Ni}$ ) in the deviations, which explains why the large deviations seen in Fig. 8 are not in contradiction with a least-square fit to the binding energies of a few selected nuclei.

Note that SLy4 has been adjusted to magic nuclei for which there are no pairing correlations present at the BCS level of approximation. With our LN+projection scheme, pairing correlations are present even in doubly magic nuclei. It increases in particular the binding energy of the lightest doubly-magic nuclei in the sample of fit nuclei.  $^{40}\text{Ca}$  and  $^{48}\text{Ca}$  were already over bound by 2.18 MeV and 1.88 MeV, respectively, and pairing adds about another MeV for  $^{48}\text{Ca}$  and about 1.5 MeV for  $^{40}\text{Ca}$ .

In section VI B, we shall discuss the effect of refit of a refit the parameters of the Skyrme interaction to try to minimize the rms residual or some other measure of the quality of the theory. With this linear refit of the SLy4 interaction the rms residual are decreased to 1.8 MeV, much better than the result of the liquid drop model, but still far from the accuracy of the theories with additional phenomenological terms in the energy functional.

## B. Correlation Energies

We have calculated the correlation energies for 605 even-even nuclei, including the 546 nuclei that have been

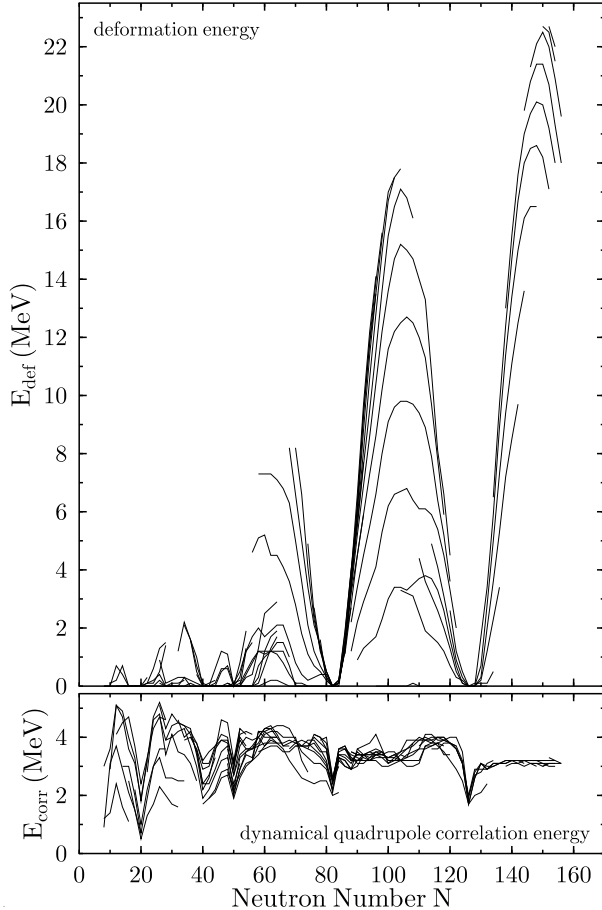


FIG. 9: The upper panel shows the static deformation energy has a function of neutron number  $N$ . Isotopic chains are connected by lines. The lower panel gives the correlation energy including angular momentum projection and mixing deformations. Note that the panels share the same energy scale.

measured (to a precision of 200 keV or better). They are available from the Physical Review archive [64] as well as from our own web site [65].

Figure 9 shows how static and dynamical quadrupole correlations enter into the total binding energies. In the upper panel are plotted the static deformation energies. Note that they include automatically contributions from all multipoles  $Q_{\ell 0}$  with even  $\ell$ .

Both static and dynamic correlation energies are close to zero for doubly-magic nuclei and increase rapidly away from closed shells to be maximum mid-shell. In light nuclei, the static correlation energy never exceeds a few MeV while it grows up to 18 MeV for  $A$  between 150 and 180 and actinides. This energy gain is typical for non-relativistic interactions, as illustrated by Figure 16 in Ref. [1], while it is only around 5 MeV for relativistic Lagrangians for  $^{240}\text{Pu}$ . On the other hand, the dynamical correlation energy is close to 4 MeV for mid-shell nuclei and decreases slightly for heavy ones. However, static and dynamical correlations behave differently: the latter

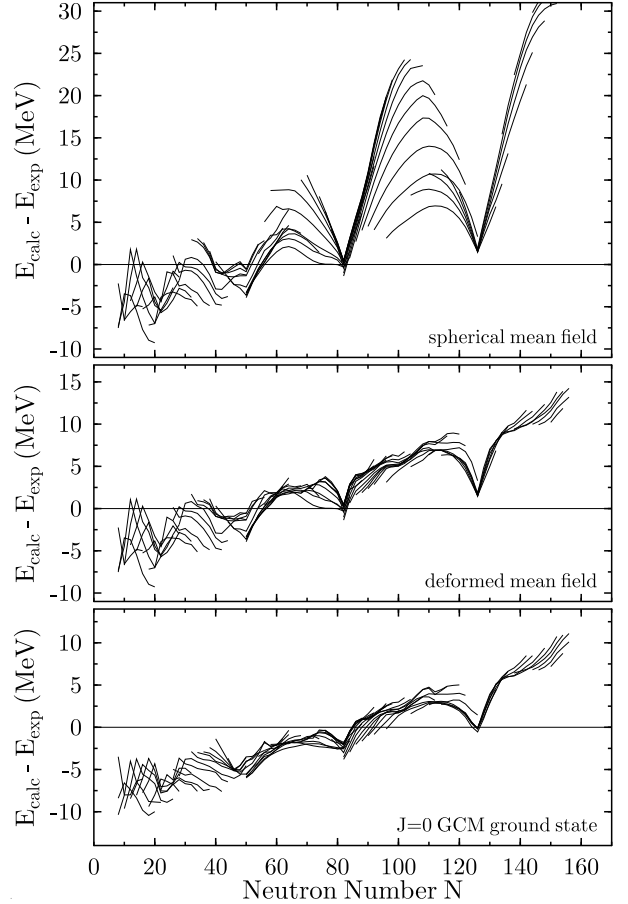


FIG. 10: Deviation of spherical mean-field (top panel), deformed mean-field (middle panel) and  $J = 0$  projected GCM energies from experiment. Positive residuals denote under-bound nuclei. Note that all panels share the same energy scale. Isotopic chains are connected by lines.

are significant as soon as the nucleus is not a doubly magic one, while the former sets in only in nuclei with a larger number of protons and neutrons in the open shell. This has some consequences for mass systematics around closed shell, as we will discuss it below.

The results plotted in Fig. 9 are in agreement with the usual assumption that the mean-field approximation is better justified in heavy nuclei. For heavy open-shell nuclei with large symmetry breaking, a large fraction of quadrupole correlations are static and already included at the mean-field level. Dynamical correlations dominate the quadrupole energy only in light systems or around closed shells.

Figure 10 illustrates how the mass residuals are affected by quadrupole correlations. The top panel shows the deviation from experiment when spherical symmetry is imposed on the mean-field. The middle panel, identical to Fig. 8, includes static correlations by allowing for a deformed mean-field. In the bottom panel, dynamical correlations from projection on  $J = 0$  and GCM are included. The difference between the two upper panels is

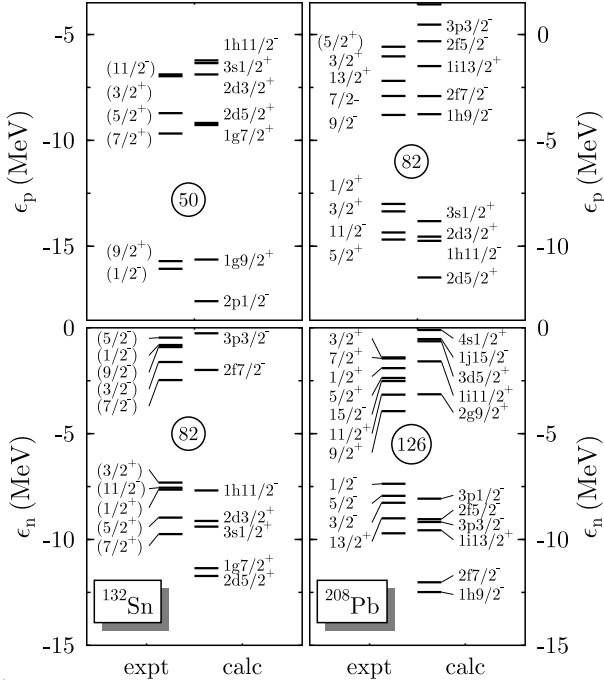


FIG. 11: Comparison between calculated (right) and experimental (left) single-particle spectra of protons (top panel) and neutrons (bottom panel) for  $^{132}\text{Sn}$  and  $^{208}\text{Pb}$ . See Ref. [1] for the determination of experimental values.

given by the upper panel in Fig. 9, while the difference between the two lower panels is given by the lower panel of Fig. 9. As can be expected from the systematics of deformation energies, to restrict the mean field to spherical shapes causes huge fluctuations of the mass residuals for heavy open shell nuclei. These fluctuations are not removed completely by static deformations, but their amplitude and their spread decreases, leaving a plateau for open-shell nuclei. The curves for all isotopic chains nearly fall on top of each other. The deviation between theory and experiment has now a structure where medium and heavy mid-shell nuclei fall close to a straight line, while there remain deep localized ravines around the heavy neutron shell closures  $N = 50, 82$  and  $126$ , and more irregular fluctuations in light systems. Similar results have been obtained for other effective interactions, see [54] and references therein.

One can assume that the wrong global trend with  $A$  and the deep ravines around shell closure are correlated to the procedure used to adjust effective interactions like SLy4.  $^{208}\text{Pb}$  is the only heavy nucleus included in the fit. A slight error on the volume energy coefficient of this interaction leads to an underestimation of more than 10 MeV of the masses of heavy nuclei. Since  $^{208}\text{Pb}$  is the only heavy nucleus included in the fit and since its mass is imposed, the error due to the volume energy is compensated by a too strong shell effect in  $^{208}\text{Pb}$ .

The additional binding in magic and near-magic nuclei has of course its origin in shell structure. Hence, single-

particle spectra might offer a key to the understanding of the relative overbinding of doubly-magic nuclei. The single-particle energies  $\epsilon_k$  for  $^{132}\text{Sn}$  and  $^{208}\text{Pb}$  are shown in Fig. 11. While the  $\epsilon_k$  are not truly physical quantities, there certainly is an approximate correspondence to single-nucleon separation energies and the spectra of nuclei that differ from doubly-magic ones by one nucleon. In this spirit the experimental single-nucleon separation energies are given as “expt” in the graph. For a comparison between calculated values and experiment one has to keep in mind that corrections to the  $\epsilon_k$  usually increase the level density around the Fermi energy [62, 63].

The SLy4 interaction gives in general a reasonable account of the single-particle levels and their ordering around the magic gaps, as do most SMCF functionals [1]. There are, however, inaccuracies in details. For example, the magnitude of the gap at  $N = 126$  is strongly overestimated, while the gaps at  $N$  and  $Z$  equal to 82 appear to be more realistic. The ordering of the levels below the  $N = 82$  gap in  $^{132}\text{Sn}$  is difficult to reproduce by mean-field models. SLy4 puts the  $1h_{11/2}^-$  level above the  $2d_{3/2}^+$ , while experiment gives the opposite ordering. SLy4 shares this deficiency with virtually all successful parameterizations of Skyrme as well as Gogny interactions and the relativistic mean field Lagrangians, see [1]. Its consequences for quadrupole correlations cannot be easily assessed. Another salient feature of Fig. 11 is that the calculated level density of neutrons above the  $N = 82$  gap in  $^{132}\text{Sn}$  and the  $N = 126$  gap in  $^{208}\text{Pb}$  is much lower than the experimental one, which might be one of the causes for the under-binding of nuclei above  $N = 82$  and  $N = 126$ .

The arches that we obtain are still present if the effective interaction is adjusted to all known masses and has a better volume energy coefficient. However, the amplitude of the arches is much smaller as can be seen, for example, in Fig. 3 of Ref. [59]. Dynamical quadrupole correlations reduce the fluctuations by approximately a factor 2, suggesting that their integration in a global fit of the effective interaction might bring a good agreement with the data.

Plotting mass residuals for isotopic chains as a function of  $N$  is the usual way to proceed (see, e.g., Ref. [54]). The plot of the same results for isotonic chains as a function of  $Z$ , however, leads to a very different perspective on the deviations between theory and experiment, as can be seen in Fig. 12. It demonstrates that some caution is necessary before drawing conclusions. Although the lines which connect nuclei with constant  $N$  are not perfectly horizontal, the fluctuations of the residuals around proton shell closures are much smaller at the mean-field level around neutron shell closures, and are further reduced when dynamical correlations are included. The good description of relative energies within a given isotonic chain explains why the curves for isotopic chains in Fig. 10 nearly fall on top of each other. In contrary, the staggering of the curves for isotonic chains in Fig. 12 reflects the drift of the mass residuals along isotopic chains

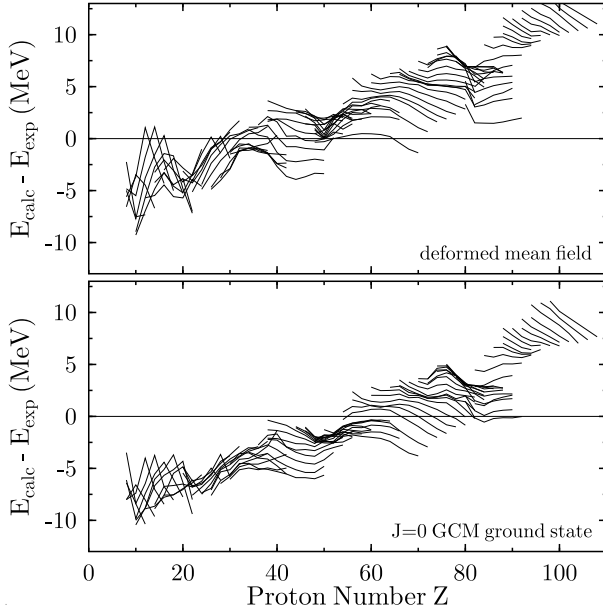


FIG. 12: Residuals of the (deformed) mean-field energy (top), and the  $J = 0$  projected GCM energy (bottom) drawn as a function of proton number. Isotonic chains are connected by solid lines.

visible in Fig. 10.

More surprisingly, there is no large missing proton shell effect, hence the deep ravines see in Fig. 10 are not representative for shells in general. It is difficult to imagine that close to the stability line there are large correlation effects related to neutron shells, but not to proton shells. We have seen in Fig. 11 that single-particle energies of protons are better described than those of neutrons. This suggests that the remaining large fluctuations of the mass residuals around magic neutron numbers are due to a deficiency of the Skyrme energy functional for current parameter sets, and not the manifestation of large missing correlations. The arches can still be identified in the mass residuals of Skyrme interactions fitted to all available masses using approximate correlation energies, see, e.g., Fig. 3 of [59].

The same data also can be drawn versus mass number as in Figures 13. The lines with constant  $N - Z$  in Fig. 13 connect nuclei in  $\alpha$ -decay chains. The horizontal lines for the heaviest nuclei indicate that  $Q_\alpha$  values are well described, as was first noticed in Ref. [66]. Otherwise, the residuals show the same problems that we found in the plot with respect to neutron number.

Next we show a plot of the isobaric chains as a function of  $N - Z$ , Fig. 14. This clearly shows a strong cusp of the residuals in light nuclei at  $N = Z$ , which are underbound relatively to the other members of isobaric chains. It clearly points out that a Wigner energy term is missing in our model. The amplitude of the fluctuation of the residuals around  $N = Z$  suggests a Wigner energy of the order 5 MeV for the lightest nuclei, and decreasing rapidly with the mass number. Note that the amplitude

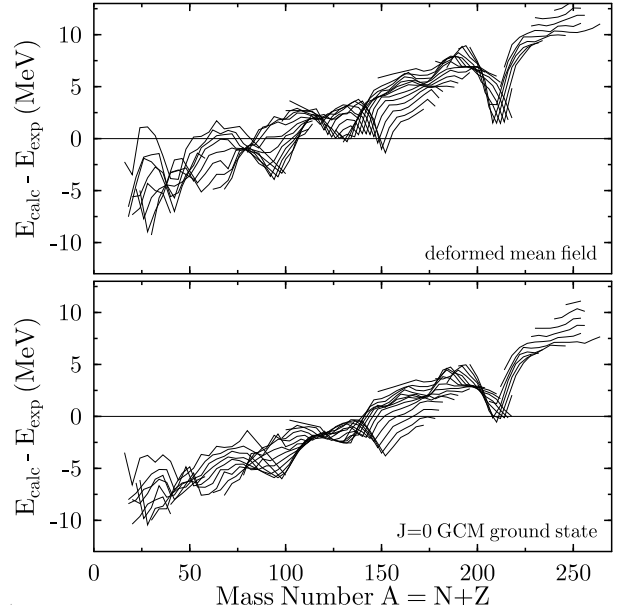


FIG. 13: Deviation of the (deformed) mean-field energy (top), and the  $J = 0$  projected GCM energy (bottom) from experiment, drawn as a function of proton number. Isotonic chains are connected by solid lines.

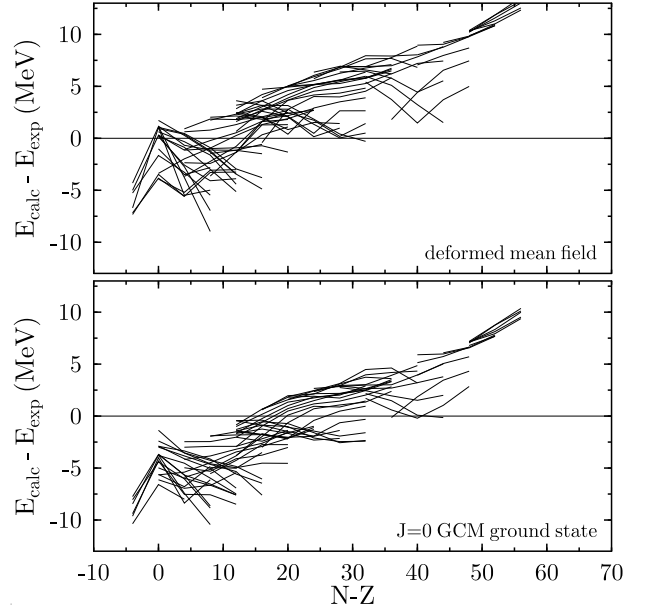


FIG. 14: Deviation of the (deformed) mean-field energy (top), and the  $J = 0$  projected GCM energy (bottom) from experiment, drawn as a function of  $N - Z$ . Only isobaric chains with  $A = 4n$  are drawn, i.e., those containing an  $N = Z$  member. Isobaric chains are connected by solid lines.

of the peaks is modified when dynamical correlations are included, as the  $N = Z$  line contains many mid-shell nuclei that have more correlation energy.

Apart from fluctuations correlated to the neutron shell closures, the trend with  $A$  is mainly linear. The refit

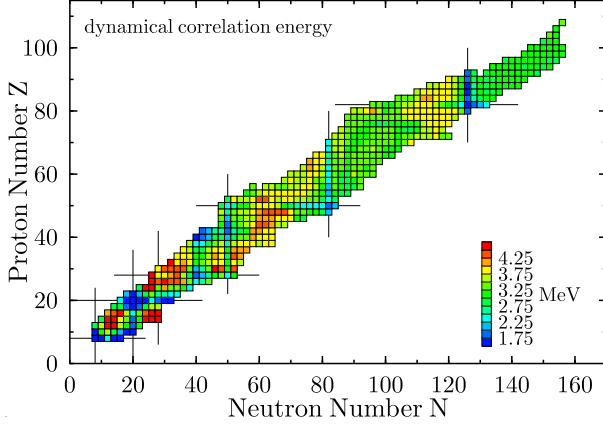


FIG. 15: Contour map of the dynamical quadrupole correlation energy in MeV.

of SLy4 presented in Ref. [13] indeed removes the trend with  $A$  with a 0.09 MeV increase of the SLy4 volume

energy coefficient  $a_{\text{vol}}$ . With this increase of  $a_{\text{vol}}$ , one gains about 21.5 MeV when going from  $^{16}\text{O}$  to a nucleus with  $A \approx 250$ , precisely what is needed to correct the slope of the residuals that one can see in all Figures.

The contour map of the dynamical quadrupole correlation energy is shown in Figure 15. It presents structures correlated to shell effects. The smallest correlation energies are obtained for magic-nuclei and the largest for transitional nuclei in the vicinity of shell closures. The maximum of the correlation energy decreases slightly with  $A$ . The correlation energy is nearly constant for rare-earth and actinide nuclei which have all a static deformation.

The  $N = 28$  shell closure is only clearly visible around  $^{48}\text{Ca}$ , the dynamical correlation energy increasing very rapidly when going away from  $Z = 20$ . This result is consistent with the disappearance of the  $N = 28$  shell effect below  $^{48}\text{Ca}$ . All the other neutron magic numbers are predicted to be very stable with only marginal changes of the correlation energy for each of them.

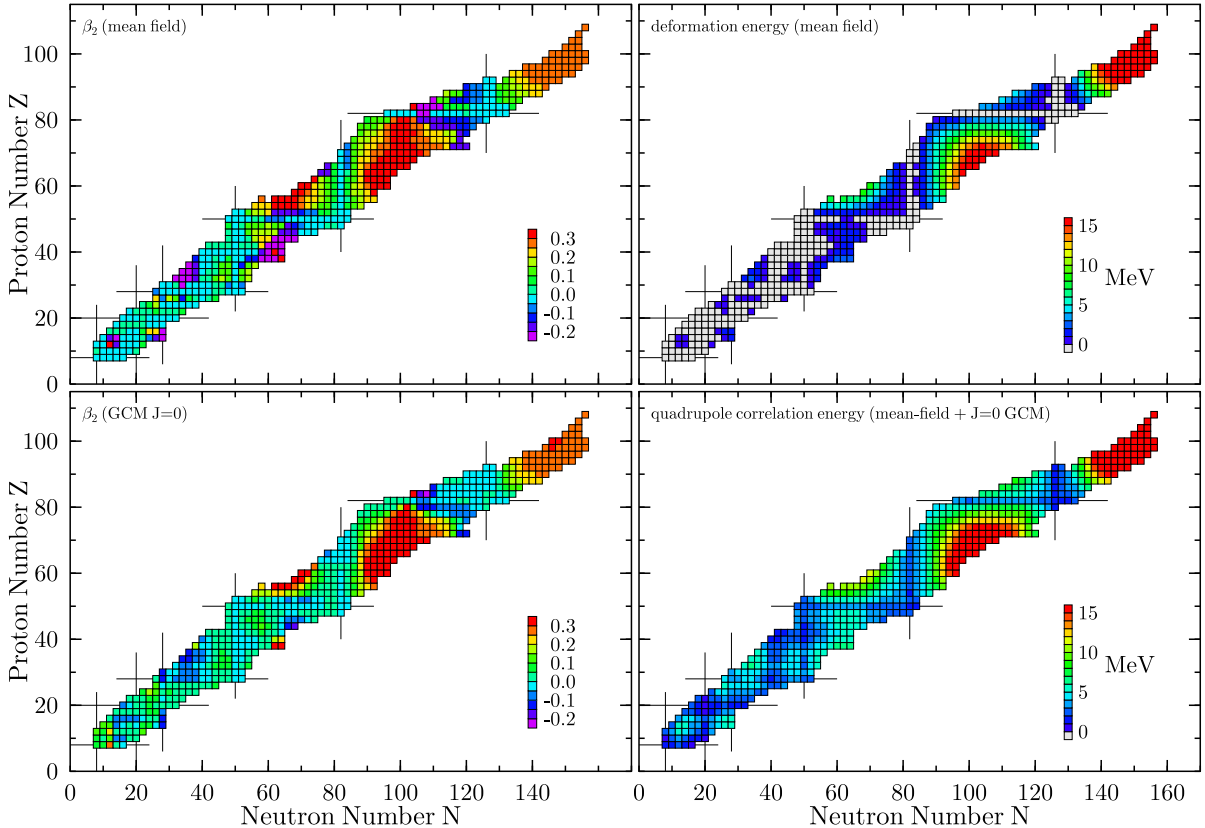


FIG. 16: Left panels: deformation of the mean-field ground state (top) and average deformation of the  $J = 0$  projected GCM ground state (see Eqn. 25). Right panels: static deformation energy of the mean-field ground state (top) and total (static+dynamic) correlation energy of the  $J = 0$  projected GCM ground state.

The situation is different for proton shells. The correlation energy is quite small around doubly-magic nuclei, but rises substantially when going along the shell to mid-neutron-shell nuclei as one can see for the Ni ( $Z = 28$ ), Sn ( $Z = 50$ ), and Pb ( $Z = 82$ ) chains. One might suspect that this asymmetry between neutron and proton shells is an artifact of the too strong neutron shell effect that has already been noticed. Because of the too strong neutron shell closures, the potential landscapes are too stiff, preventing any substantial dynamical correlations. We will come back to this point when discussing mass differences.

Figure 16 summarizes the influence of static and dynamic quadrupole correlations on the ground state wave function and on its energy. The left panels show the average intrinsic deformation of the mean-field (top) and of the correlated ground states (bottom), while on the right panels are plotted the static deformation energy (top) and the total quadrupole correlation energy. With SLy4 and our treatment of pairing correlations, most light nuclei have spherical mean-field ground states (gray squares in the upper right panel). For nuclei above  $Z = 50$ , there are three regions clearly visible of well-deformed prolate nuclei (red squares in the left panels) centered around nuclei that are mid-shell for protons and neutrons, i.e. the rare earths between  $^{132}\text{Sn}$  and  $^{208}\text{Pb}$ , their cousins with the same  $Z$  on the proton-rich side of the  $N = 82$  shell, and the actinides to the northeast of  $^{208}\text{Pb}$ . The prolate deformation of rare-earths and actinides is well-established experimentally. The structure of nuclei with large static deformation energy is not affected by dynamical correlations. The situation is different for nuclei at the outer limits of the deformed regions. There, prolate and oblate, or prolate and spherical minima coexist and are nearly-degenerate. The GCM ground state is then a mixing of a large number of configurations, with an average intrinsic deformation smaller than the mean-field ground state.

For light nuclei, the mean-field calculations hint at two regions of well-deformed oblate nuclei with  $Z \approx 34$  to the left and right of the  $N = 50$  shell closure. On the proton-rich side, this is in contradiction with experiment. The Kr isotopes, for example, are known to have prolate ground states with coexisting excited oblate structures down to  $^{74}\text{Kr}$ ; only  $^{72}\text{Kr}$  has an oblate ground state. In calculations with SLy4, the oblate minimum is always more bound, which might be related to a deficiency in the spacing of single-particle states in the  $pf$  shell obtained with this interaction.

Some Sn and Pb isotopes have small ground-state deformation after projection but before configuration mixing. This is the case when the mean-field energy surface is soft, a deformed configuration leading to a small energy gain on the order of 100 keV. After configuration mixing, however, one obtains a ground-state wave functions that has zero deformation on the average – as expected. We remind the reader again that  $\bar{\beta}_2$  does not have a physical significance when the deformation is weak.

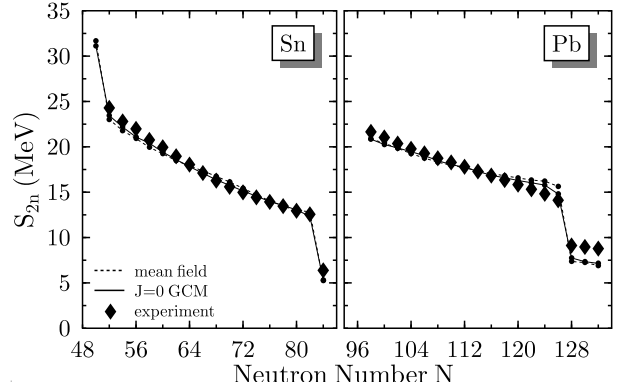


FIG. 17: Two-neutron separation energy for the Sn and Pb isotopic chains.

### C. Mass differences

In many applications, it is not masses themselves that are important but differences between masses, as separation energies or  $Q$  values. We have shown that dynamical correlation energies change abruptly around shell closures and this should have a visible effect on mass differences. Let us look first to two-nucleon separation energies

$$\begin{aligned} S_{2n}(N, Z) &= E(N - 2, Z) - E(N, Z) \\ S_{2p}(N, Z) &= E(N, Z - 2) - E(N, Z). \end{aligned} \quad (27)$$

They represent first order derivatives of the masses along isotopic and isotonic chains.

Figure 17 shows the  $S_{2n}$  for the chain of tin and lead isotopes. All tin isotopes have spherical mean-field ground states, and the average intrinsic deformation of the  $J = 0$  GCM states remains close to zero. Dynamical correlations always bring some gain of energy but which varies slowly for the open-shell isotopes and energy differences are then marginally affected. The already good agreement with data at the mean-field level is slightly improved by correlations, in particular for the light isotopes and around  $N = 70$ , for which the potential landscapes are rather soft. The only large change is obtained for closed-shell nuclei  $^{100}\text{Sn}$  and  $^{132}\text{Sn}$ , for which the quadrupole correlation energy is smaller than for neighboring nuclei by about 1 MeV and the “jump” in the  $S_{2n}$  is reduced at the shell closure. The  $S_{2n}$  in Pb isotopes are also not much affected by correlations. In particular, the excessive jump around  $N = 126$  is not sufficiently reduced by correlations.

More complex examples are the chains of Dy and Th isotopes for which both static and dynamical quadrupole correlations are large. In both chains, the  $S_{2n}$  shown in Fig. 18 deviate from the experimental values by at least 2 MeV when spherical symmetry is imposed. Allowing for deformations significantly improves the agreement with experiment. To obtain such an effect, the deformation energy has to change by about 2 MeV from one isotope to the next, as it is seen in the upper panel of Fig. 9.

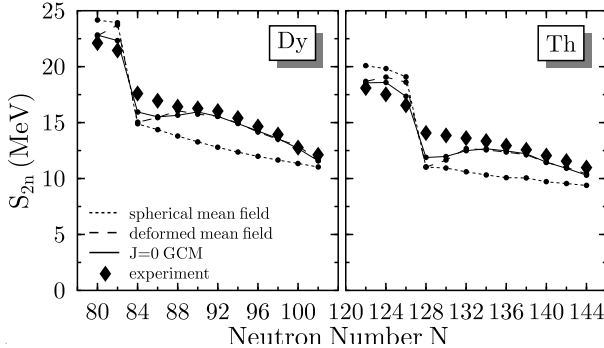


FIG. 18: Two-neutron separation energy for the Dy ( $Z = 66$ ) and Th isotopic ( $Z = 90$ ) chains.

The deformation energy increases rapidly on both sides of a magic number, but its derivative has a different sign above and below; therefore deformation decreases the  $S_{2n}$  below a magic number, and increases it above. Going to  $N$  values larger than the magic number, the  $S_{2n}$  curve obtained when deformation is allowed will eventually cross the spherical curve, when the deformation energy will be decreasing again with  $N$ . The dynamical correlations improve the  $S_{2n}$  further around the  $N = 82$  (Dy) and  $N = 126$  (Th) shell closures, in particular below them. Note that the influence of dynamical correlation energies on separation energies is necessarily quite localized, as correlations saturate just a few mass units away from shell closures. The remaining discrepancy just above the  $N = 126$  shell closure leaves room for octupole correlations, which are known to be particularly strong in this mass region [67].

To amplify the change of masses around shell closures even further, one can study the so-called two-nucleon gaps

$$\begin{aligned}\delta_{2n}(N, Z) &= E(N, Z - 2) - 2E(N, Z) + E(N, Z + 2) \\ \delta_{2p}(N, Z) &= E(N - 2, Z) - 2E(N, Z) + E(N + 2, Z),\end{aligned}\quad (28)$$

which are equivalent to second order partial derivatives of masses as a function of  $N$  or  $Z$ . In a mean-field model,  $\delta_{2p}(Z)$  can be approximated by twice the difference of the Fermi energies between two nuclei differing by two neutrons or two protons, provided that all nuclei entering Eqn. (28) have the same structure. For magic nuclei, this quantity is also approximated by twice the gap in the single-particle spectrum. For this reason, the two-nucleon gaps are often used as signatures for magicity.

Figure 19 shows the two-proton gaps  $\delta_{2p}$  along the  $N = 82$  and  $N = 126$  isotonic chains. Except for the doubly-magic  $^{132}\text{Sn}$  ( $Z = 50$ ) and  $^{208}\text{Pb}$  ( $Z = 82$ ), the description of experiment by mean-field calculations is quite good. Dynamical quadrupole correlations modify the  $\delta_{2p}$  mainly around the proton shell closure, where the systematics does not necessarily improve. The  $\delta_{2p}$  at the magic number  $Z$  decreases, as it does at  $Z + 4$ , while it

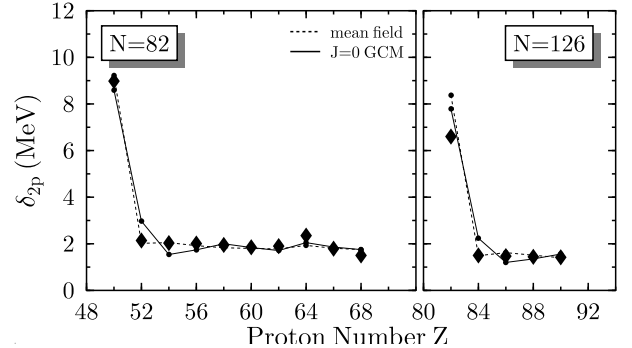


FIG. 19: Two-proton gaps for  $N = 82$  and  $N = 126$  isotonic chains.

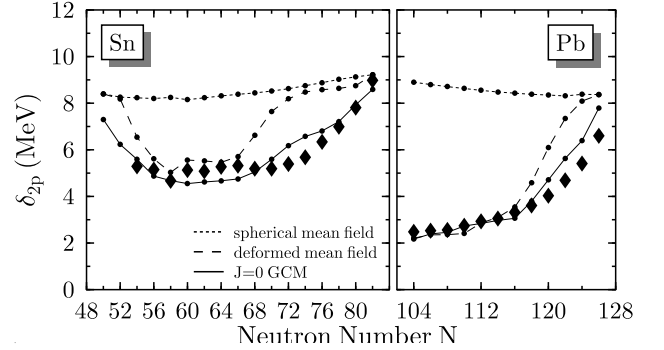


FIG. 20: Two-proton gaps for Pb and Sn isotopic chains. Experimental data are represented by filled diamonds.

increases for  $Z + 2$ . As a result, the mean-field agreement with experiment at the mean-field level for  $Z + 2$  and  $Z + 4$  is slightly marred by dynamical correlations.

The two-particle gaps across a magic number are known to be difficult to describe by mean-field models. Experimentally, shell effects are enhanced when both neutrons and protons form closed shells, a phenomenon called “mutually enhanced magicity” [68, 69] that cannot satisfactorily be described in a mean-field picture. It may be seen in Fig. 20, where the two-proton gaps for the  $Z = 50$  (Sn) and  $Z = 82$  (Pb) isotopic chains are plotted as a function of  $N$  rather than  $Z$ . Now  $\delta_{2p}$  represents the magicity of the proton shell when  $N$  is varied. The cases of Sn and Pb have gained considerable attention, as the experimental data clearly show a large reduction of the  $\delta_{2p}$  when going away from the doubly-magic  $^{132}\text{Sn}$  with 82 neutrons and doubly-magic  $^{208}\text{Pb}$  with 126 neutrons. The reduction is particularly large for the neutron-deficient Pb isotopes, which led to some speculations about a possible quenching of the  $Z = 82$  shell far from stability.

The SCMF gives quite flat predictions for  $\delta_{2p}$  in the spherical approximation, as shown by the dotted line in the figure. This reflects the independence of the gap in the single-particle spectrum of the protons on the neutron number for spherical nuclei [70]. Allowing for static deformation leads to a change in the right direction. It

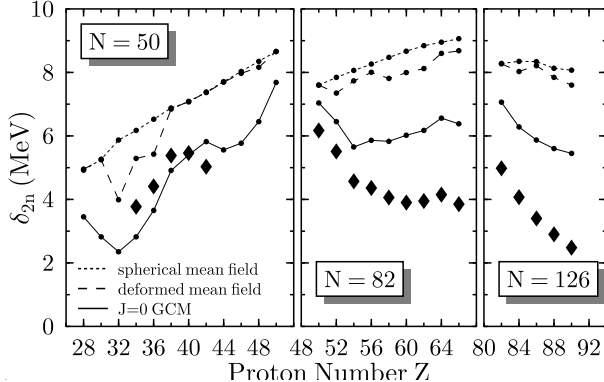


FIG. 21: Two-neutron gaps for  $N = 50$ ,  $N = 82$  and  $N = 126$  isotonic chains.

is of course not the Sn and Pb isotopes which gain deformation energy, but nuclei in the  $Z \pm 2$  chains. Adding dynamical quadrupole correlations brings the calculated curve very close to the experimental one. Again, this is due to nuclei in the  $Z \pm 2$  chains, which are softer than the magic ones and therefore gain more dynamic correlation energy. Similar results for the  $\delta_{2p}$  in the Sn chain have been recently obtained with a microscopic Bohr Hamiltonian based on a different Skyrme interaction [49].

While the correlation energy gives quite a significant qualitative and quantitative improvement of finite-mass-difference formulae along the direction of changing proton number, the situation is less satisfactory along changing neutron numbers. Figure 21 shows as an analogue to Fig. 20 for neutrons the two-neutron shell gap  $\delta_{2n}$  across the  $N = 50$ ,  $N = 82$  and  $N = 126$  isotonic chains. As in the case of proton shells in Sn and Pb, the experimental values for neutron shell gaps are reduced when going away from the shell closures. In comparison to the proton case there remain, however, large deviations from experiment. Values for  $\delta_{2n}$  calculated from spherical mean-field states are flat only for  $N = 126$ . They vary rapidly for the other two chains although in the wrong direction with respect to the data for  $N = 82$ . Allowing for deformation slightly reduces the  $\delta_{2n}$ , as some of the nuclei with  $N \pm 2$  are deformed. This effect is, however, much weaker than for the proton shell gaps in the Sn and Pb isotopes. The dynamical correlations reduce the  $\delta_{2n}$  for all nuclei shown by approximately 2 MeV, bringing the theory close to experiment for  $N = 50$ . This change is, however, not sufficient for the  $N = 82$  and  $N = 126$  chains. The discrepancy remains the largest for the  $N = 126$  chain with a much too large neutron shell gap in  $^{208}\text{Pb}$ .

The failure of the dynamical correlations to describe the reduction of the  $\delta_{2n}$  quantitatively reflects, of course, the ravines that remain in the lower panel of Fig. 8. This suggests that the neutron shells in heavy nuclei are too strong, while proton shells are much better described. This interpretation is supported by the comparison of the calculated single-particle spectra of heavy nuclei with experimental data that we already discussed in Fig. 11.

TABLE V: RMS residuals of the binding energy and various binding energy differences for spherical mean-field states, mean-field ground states, and the  $J = 0$  projected GCM ground states as obtained with SLy4. All energies are in MeV.

Theory	$E$	$S_{2n}$	$S_{2p}$	$\delta_{2n}$	$\delta_{2p}$	$Q_\alpha$
spherical SCMF	11.7	1.6	1.6	1.2	1.1	2.1
deformed SCMF	5.3	1.1	1.0	1.2	1.1	1.1
+ $J = 0$		4.4	0.9	0.8	0.9	1.0
+ GCM		4.4	0.8	0.8	0.9	0.8

## VI. MASS-TABLE FITS

In the previous section, we discussed the effects of quadrupole correlations looking at trends with  $N$  and  $Z$  and at specific chains of nuclei. Here, we will take a more global perspective on the correlation energies, and assess their effect on the table of nuclei as a whole.

### A. Evolution of errors with the inclusion of correlations

The rms residuals obtained by adding the three components of quadrupolar correlations to the spherical mean-field values are given in Table V. Let us first discuss the evolution of residuals for binding energies, also shown as the left panel in Fig. 22. The first line corresponds to SCMF in the spherical approximation. It has an rms residual of about 12 MeV. Since the SLy4 interaction is fitted to doubly magic nuclei, this poor performance in the spherical approximation is to be expected. Incorporating axial deformations in the SCMF, the rms residual improves to 5.3 MeV. The next line shows the results obtained by adding  $E_{J=0}$  to the mean-field energies. The angular momentum projection gives a 20 % improvement in the rms residual. This is not surprising; having only fit magic nuclei, a correlation effect that is stronger for mid-shell nuclei has a good chance to improve the overall agreement. The last line shows the effect of incorporating the full correlation energy. It does not improve the residuals as compared to the inclusion of  $E_{J=0}$  only.

This last result may seem disappointing: the "best" calculation does not give better residuals for binding energies than calculations which do not include the correlations due to configuration mixing. The most obvious factor accountable for this failure is that the effective interaction that we use has been adjusted at the mean-field level. Correlation energies always increase the binding energies. Since with SLy4 light nuclei are already predicted over-bound by the deformed mean-field ground state, correlations only worsen the situation, as can be seen in Fig 10. Therefore the correlations cannot improve the binding energy residuals.

To check this conclusion, we also give the rms deviations for several energy differences of interest in Table V,

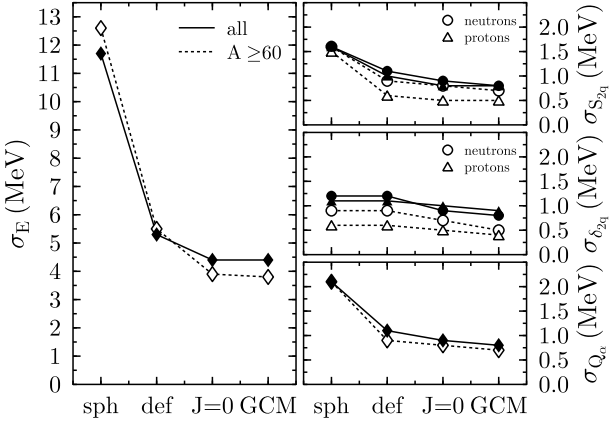


FIG. 22: RMS residuals between theory and experiment in different approximations. Left panel: rms residuals of the masses with the SLy4 interaction when going from spherical SCMF (sph) to the SCMF ground state (def), the  $J = 0$  projected minimum ( $J = 0$ ) to the  $J = 0$  projected GCM ground state (GCM). Filled markers denote values for all nuclei in our sample, open markers heavy nuclei with  $N, Z > 30$  only. The lines are to guide the eye. Right panels: corresponding two-nucleon separation energies  $S_{2n}$  and  $S_{2p}$  (top), two-nucleon gaps  $\delta_{2n}$  and  $\delta_{2p}$  (middle) and  $Q_\alpha$  values (bottom).

also shown in Fig. 22. The spherical mean-field values for  $S_{2n}$ ,  $S_{2p}$  and  $Q_\alpha$  are substantially improved by static quadrupole correlations, while the two-nucleon gaps  $\delta_{2n}$  and  $\delta_{2p}$  are nearly unaffected. The deviations at the deformed mean-field level are slightly larger than 1.0 MeV for the five energy differences. The next two lines of the Table show the effect of including  $E_{J=0}$  and  $E_{GCM}$ . In all cases, one sees a significant improvement ranging from 15 % to 30 %. These results are encouraging to demonstrate a role for correlation effects, but to make a firm conclusion on the need for the correlation energies one should refit the parameters of the SCMF and show that the improvement remains when the parameters are separately optimized with and without the correlations. We will come to this in a later section.

For the two-nucleon gaps  $\delta_{2n}$  and  $\delta_{2p}$  the static deformation brings no measurable improvement of the rms residuals, while the dynamical correlations do. This reflects that the two-nucleon gaps are a filter for discontinuities in the systematics of masses. The static deformation energy does not exhibit any noticeable discontinuities, it only moderately smooths the discontinuity from the spherical mean field. Therefore it has no visible effect on the rms residuals of the  $\delta_{2n}$  or  $\delta_{2p}$ . In contrast, the dynamical correlation energy obviously has a kink at magic numbers, as illustrated by Fig. 9. As the most prominent discontinuities of the dynamical correlation energy and the mean-field coincide, there is a visible effect of the dynamical quadrupole correlations on the  $\delta_{2n}$  and  $\delta_{2p}$ .

While the fluctuations of the rms residuals in heavy nuclei are mainly correlated to magic numbers, they ap-

TABLE VI: The same as table V, but for heavy nuclei with  $N, Z > 30$  only.

Theory	$E$	$S_{2n}$	$S_{2p}$	$\delta_{2n}$	$\delta_{2p}$	$Q_\alpha$
spherical SCMF	12.6	1.6	1.5	0.9	0.6	2.1
deformed SCMF	5.5	0.9	0.6	0.9	0.6	0.9
+ $J = 0$		3.9	0.8	0.5	0.7	0.5
+ GCM		3.8	0.7	0.5	0.5	0.7

pear to be much more random in light nuclei, in part due to the additionally missing Wigner energy, c.f. Fig. 14. The missing contribution to the energy appears to reach as far as ten mass units from the  $N = Z$  line. As our model cannot describe the effect that leads to the Wigner energy, we cannot expect to obtain a satisfactory description of light nuclei. The peak in the energy residuals from the missing Wigner energy causes a slope and a discontinuity in the energy residuals, therefore it affects particularly separation energies and two-nucleon gaps. Indeed, when removing light nuclei with  $N, Z < 30$  from the calculation of the rms residuals, the overall description of mass differences appears to be much better, see Table VI.

## B. Refits of the SCMF interaction

In this subsection we will refit the parameters of the Skyrme interaction to see the quality of the binding energy fits that can be achieved with SCMF. Table V showed that the correlations are helpful for the SLy4 energy functional, but that parameterization was never optimized to binding energies. Thus, we should ask whether the theory does better with the computed correlation energy if the parameters are optimized by refitting both cases. As a full fit of a Skyrme interaction to all nuclear masses is too costly to be performed with the correlation energy included, we will follow here the procedure of Ref. [13] to readjust the parameters of the SLy4 functional perturbatively. Our conclusions will have to be tentative because the pairing part of the functional was not refitted, and because the perturbatively refit will not catch a better fit that is very different from the starting point.

The perturbative refit is performed as follows. The SCMF energy is decomposed into a sum of integrals, each of which is proportional to some linear combination of the Skyrme parameters. Because of the variational property of the self-consistent mean-field theory, these integrals and the residuals are all that is needed to perform a linear refit of the Skyrme parameters to minimize the root-mean-square residual or some other measure of the fit. The only point causing difficulty is the redundancy of the Skyrme parameters. Certain linear combinations of these parameters are very poorly determined by nuclear masses, and should not be included in the fit. Accord-

TABLE VII: Quality of binding energy fits for various treatments of effects beyond mean field. The first line show the SCMF with particle number projection and below that are the results including successively particle number angular momentum projection, and mixing of deformations by the GCM. All energies are in MeV.

Theory	rms residual	C-norm
deformed SCMF	1.83	5.40
+ $J$ projection	1.70	4.96
+ GCM	1.72	5.01

TABLE VIII: Quality of fits to separation energies and two-nucleon gaps fits for various treatments of effects beyond mean field, as in Table VII.

Theory	$S_{2n}$	$S_{2p}$	$\delta_{2n}$	$\delta_{2p}$
deformed SCMF	1.03	0.90	1.02	1.06
+ $J$ projection	0.85	0.77	0.90	0.92
+ GCM	0.79	0.72	0.83	0.84

ing to Ref. [13], only four combinations out of the ten parameters are well fixed by the binding energies, and a corresponding singular value decomposition of the fitting matrix is needed. In Ref. [13], the energies were computed with the code `ev8`, but, as explained in Sect. II A, the code `promesse` used here is more accurate.

In Table VII, we show the results of the fits optimizing the rms residuals of the binding energies, starting with the SCMF allowing static deformations. The refitting of the SLy4 Skyrme parameters gives a very large improvement on the binding energy residuals, reducing the rms of the SCMF by a factor of three to 1.8 MeV. The  $J = 0$  projection lowers the rms residual in a refit by 0.13 MeV, while a refit adding as well  $E_{\text{GCM}}$  lowers it by 0.11 MeV. Thus, a better fit can be obtained with the correlation energies than without them, justifying the program of going beyond SCMF in this way. The situation looks better when we examine fits to mass differences, which are less sensitive to the SCMF. These are shown in Table VIII. At the level of the SCMF, the effect of a refit is quite small: 4 % improvement for the separation energies and 4 to 11 % for the  $\delta_2$ . This confirms the common assumption that the differences are quite insensitive to fine adjustments of the parameterization. For the theories including correlation energies  $E_{J=0}$  or  $E_{\text{corr}}$ , the refits improved the numbers very slightly. Thus, the results shown in Table V for the effects of the correlation energies are also valid when the parameters are readjusted in a perturbative fit. We emphasize that for the mass differences, both the angular momentum projection and the GCM mixing of configurations with different deformation give an improvement.

An alternative norm for parameter fitting is the so-called Chebyshev norm, defined as the largest residual in

TABLE IX: Critical nuclei in the perturbative minimax fits to binding energies starting from SLy4, listed by proton-neutron numbers ( $Z, N$ ).

theory	critical nuclei			
	over-bound	under-bound		
deformed SCMF	(10,18)	(82,126)	(38,38)	(38,64) (94,152)
+ $J$ projection		same	(38,38)	(38,64) (42,64)
+ GCM	(12,8)	(82,126)	(38,38)	(38,64) (74,108)

a fit performed to minimize that quantity (the “minimax” fit). In Ref. [13] it was shown that the Chebyshev norm could be more sensitive to the problems in the data set, and it also focuses on the cases most in need of attention. Fits made by refitting four well-determined vectors of SLy4 are shown in the last column of Table VII. One sees that value of the norm is about three times the rms value, and that the relative changes from one treatment of correlations to another are very similar with the two norms. It is of interest to examine the critical nuclei, namely the nuclei that have the largest residuals. For an fit with four independent vectors there are five critical nuclei, given in Table IX.

In the mean field approximation, there are two over-bound nuclei among the critical nuclei, the doubly-magic  $^{208}\text{Pb}$  and the light neutron-rich nucleus  $^{28}\text{Ne}$ . The under-bound nuclei are two nuclei along the  $N = Z$  line and a very heavy neutron-rich nucleus. With the projections and a refit of the parameters, we expect the overbinding of magic nuclei to be mitigated, but the change is not large enough to remove  $^{208}\text{Pb}$  as an over-bound critical nucleus. The under-bound nuclei are not the same, however. There is still a nucleus along the  $N = Z$  line but the others are middle-mass neutron-rich. The presence of  $N = Z$  nuclei in all lines confirms that special binding effects, the so-called Wigner energy, are present but not treated by our correlation mechanisms. We note that the phenomenological treatment of correlations in Ref. [2] made use of a Wigner energy term with several parameters.

The continued presence of  $^{208}\text{Pb}$  on the table reflects in part the special role that this nucleus plays in the construction of SLy4. A linear refit can correct the global parameters of the interaction but not the single-particle spectra and it will not decrease the too large neutron gap. On the other hand, one can also expect that the inclusion of only quadrupole axial correlations underestimates the correlation energies and that other dynamical role should play a role [71].

## VII. SYSTEMATICS OF CHARGE RADII

Correlations also may have an appreciable effect on geometrical observables such as the mean-square (ms) radius of the charge distribution  $r_c^2$ . Although deforma-

tion is not a meaningful concept for  $0^+$  states in the laboratory frame, the mean weight  $\beta_2$  of the ground state components can be substantially different from the deformation of the mean-field ground state. One can therefore expect particularly large changes of ms radii for light nuclei in general, and for heavy transitional nuclei.

### A. Procedure

To calculate the ms radius of the charge distribution, one starts from the ms radius of the point-proton distribution

$$r_p^2 = \frac{1}{Z} \langle \Phi | \hat{r}_p^2 | \Phi \rangle, \quad (29)$$

where  $|\Phi\rangle$  is either a mean-field state, a projected mean-field state or a projected GCM state. To calculate the non-diagonal matrix element of  $\hat{r}_p^2$ , we use the same method based on the topological GOA as for the Hamiltonian kernel. A comparison with radii calculated with the complete projected GCM gives us confidence that the quality of our GOA is on the order of 0.01 fm, and often much better.

The charge ms radius is then obtained by adding a correction for the finite size of the proton [1]

$$r_c^2 = r_p^2 + 0.64 \text{ fm}^2. \quad (30)$$

This correction plays no role for differences of charge radii, as for example isotopic shifts. The root-mean-square (rms) radius is obtained by taking the square root of Eqn. (30).

For nuclei whose mean-field ground state is spherical, dynamical correlations always increase the ms radius since deformed configurations contribute to the collective GCM ground state. For nuclei with a very shallow deformed mean-field minimum, as for several heavy transitional nuclei, the GCM ground state will be spread over a wide range of mean-field states, a mechanism which could lead to a reduction of the radii.

The amount of increase of radii in spherical nuclei depends on the softness of the projected energy landscapes. For light nuclei, it is particularly large, the GCM ground state being spread over a large range of deformations, as illustrated by Fig. 4. The charge radii of light nuclei might increase by more than a percent for the lightest ones, an effect which should not be neglected if their values are included in the fit of an effective interaction.

### B. Global Trends

Figures 23 and 24 show how static and dynamical correlations influence the deviation of calculated rms charge radii from experimental data, taken from a recent compilation by Angeli [72]. The error bars on rms radii are often much larger than those on masses. The values for

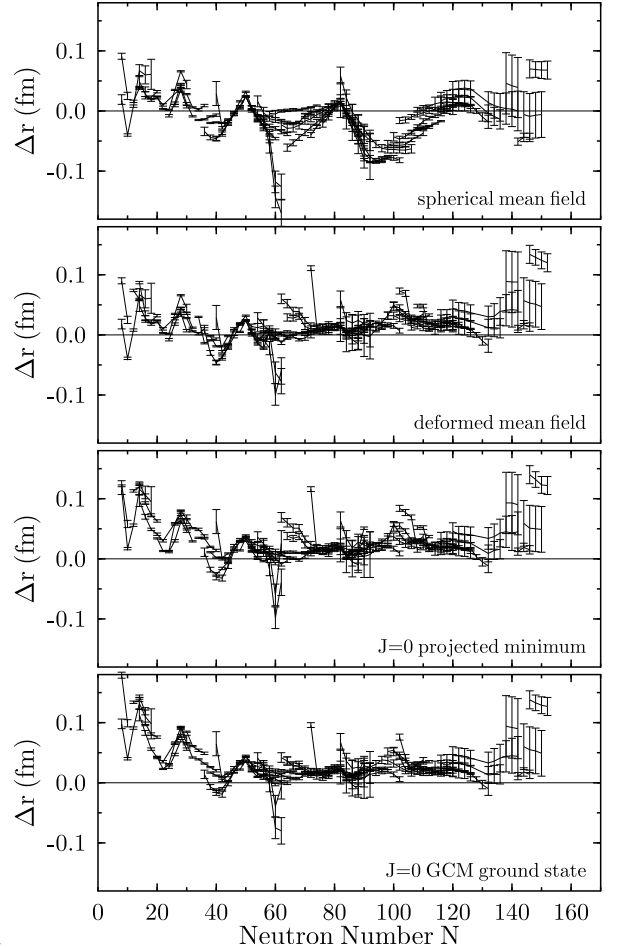


FIG. 23: Deviations of the calculated rms charge radii  $\sqrt{r_c^2}$  from experimental values as a function of neutron number. We also show the experimental error bars. Positive values denote overestimated radii. Solid lines connect nuclei in isotopic chains.

$Z = 66$  isotopes with an experimental error bar larger than 0.2 fm have been omitted from the plot. Note that the rms radius of  $^{56}\text{Ni}$ , that was used for the fit of the SLy4 interaction, is not included in [72].

The radii calculated with a mean field restricted to spherical symmetry underestimate the experimental data for open-shell nuclei, in particular for the  $N \approx 66$  region and rare-earth nuclei  $N \approx 100$ . This is expected, since these nuclei are known to be deformed. Including deformations improves the agreement with data, as can be seen in the middle panel of Figs. 23 and 24. In some mass regions, however, the rms radii are then overestimated, in particular in the vicinity of the  $Z = 82$  shell closure. This is again not too surprising, as for transitional nuclei with soft deformation energy surface, the ground state is poorly described by a single mean-field state. Dynamical correlations take into account the spread of the ground state over deformations, which often reduces the rms radii of many transitional nuclei. When these correlations are included, the agreement with data is rather

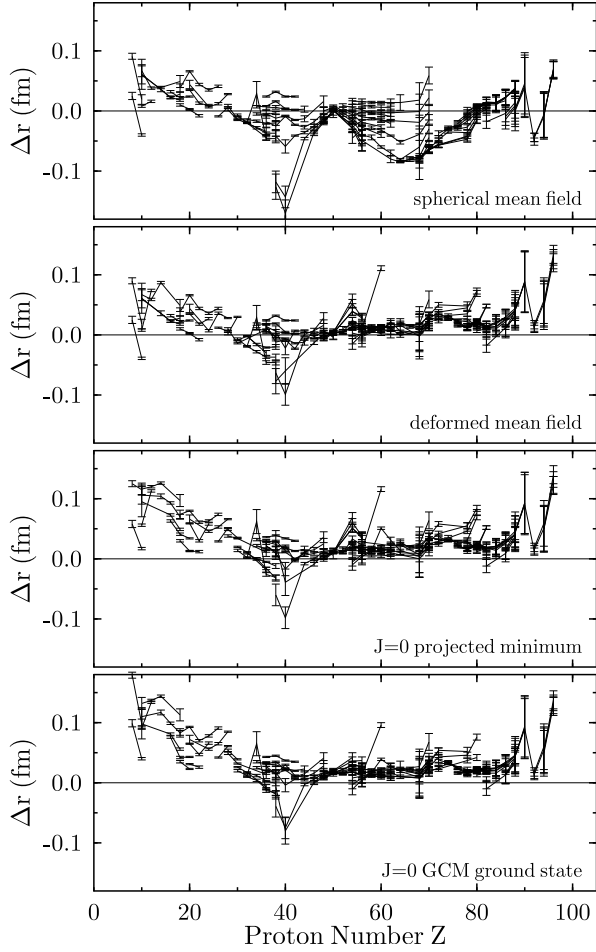


FIG. 24: The same as Fig. 23, but plotted for isotonic chains as a function of proton number.

satisfactory for most nuclei in the region between  $^{56}\text{Ni}$  ( $N = Z = 28$ ) and  $^{208}\text{Pb}$  ( $N = 126, Z = 82$ ), as can be seen in the lower panel of Figs. 23 and 24. A noteworthy exception is the neutron-rich Zr region around  $^{100}\text{Zr}$ , where the charge radii are strongly underestimated.

The situation is somewhat different for the lightest and the heaviest nuclei. The heaviest nuclei in Fig. 23 are known to be well deformed, but for some isotopic chains the radii are already overestimated by the spherical mean-field approximation and cannot be improved by the inclusion of deformations and correlations. Although our results suggest that SLy4 systematically overestimates the charge radii of heavy nuclei, a firm statement cannot be made, as, with the exception of the  $Z = 96$  chain, the experimental error bars are very large.

For light nuclei, the mean-field ground state is, in most cases, spherical. The spreading of the GCM ground-state wave functions over deformation leads then to an increase of the rms radii. As the radii of  $^{40}\text{Ca}$ ,  $^{48}\text{Ca}$ , and  $^{56}\text{Ni}$  are included in the fit of SLy4 which is done with spherical mean-field states, their radii are too large when correlations are included.

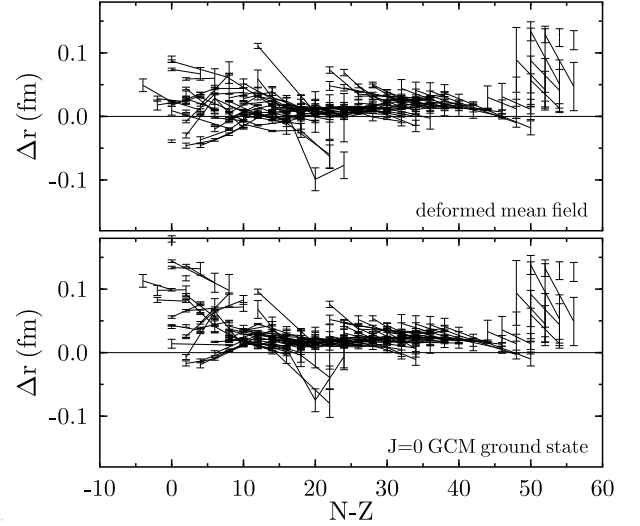


FIG. 25: The same as Fig. 23, but plotted for isobaric chains as a function of  $N - Z$ .

TABLE X: RMS residuals  $\sigma_{\text{rms}}$  and average values  $\overline{\Delta r}$  of the rms charge radii for all nuclei in our sample (left two columns) and for heavy nuclei with  $N, Z > 30$  only.

Theory	all		$N, Z > 30$	
	$\sigma_{\text{rms}}(r_{\text{rms}})$	$\overline{\Delta r}$	$\sigma_{\text{rms}}(r_{\text{rms}})$	$\overline{\Delta r}$
spherical	0.038	-0.012	0.039	-0.017
deformed	0.032	0.016	0.031	0.015
+ $J = 0$	0.041	0.027	0.034	0.022
+ GCM	0.043	0.030	0.033	0.023

Residuals for isobaric chains are plotted as a function of isospin  $N - Z$  in Fig. 25. For light nuclei, there is no significant correlation of the residuals with the  $N = Z$  line. On the other hand, for heavy nuclei, there is a clear trend that the theoretical radii do not increase fast enough with increasing asymmetry  $N - Z$ .

The rms residuals of the radii are given in the first column of Table X. There is an overall improvement when going from spherical to deformed mean-field states. Including dynamical correlations, however, increases the rms residuals again. The main reason for this result is that the average value of the residuals, defined by

$$\overline{\Delta r} = \frac{1}{N} \sum_{j=1}^N (r_{\text{rms}}^{\text{exp}} - r_{\text{rms}}^{\text{cal}}) \quad (31)$$

and given in the second column of Table X, increases from 0.016 to 0.031 when adding dynamical correlations to the SCMF ground state. The overall upward shift when going from the top panel to the bottom panel in Figs. 23 and 24 reflects the same result. The increase of the radii is the largest for the lightest nuclei in our sample. As for masses, the agreement is more satisfactory when removing the lightest nuclei with  $N, Z \leq 30$  from

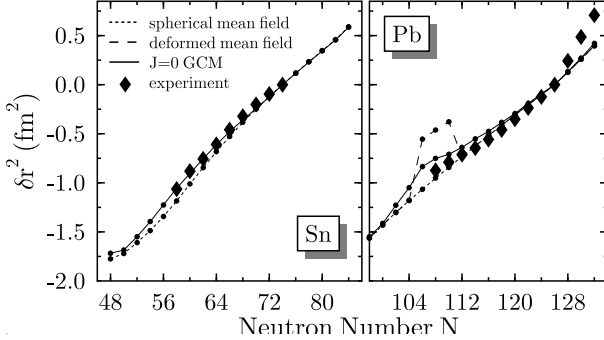


FIG. 26: Systematics of the isotopic shifts of the mean-square charge radii along the Sn and Pb isotopic chains. Isotopic shifts of Sn isotopes are with respect to  $^{124}\text{Sn}$ , in Pb isotopes with respect to  $^{208}\text{Pb}$ .

the sample as shown in the two right columns of Table X.

### C. Local trends

As dynamical correlations lead to an overall increase of the rms radii, any assessment on the role of dynamical correlations for radii cannot be made on the grounds of the rms residuals. As in the case of masses, the improvements brought by correlations are better seen when looking at isotopic shifts which are differences of radii:

$$\delta r_c^2(Z, N) = r_c^2(Z, N) - r_c^2(Z, N_0). \quad (32)$$

In Fig. 26, the isotopic shifts for the chains of Sn and Pb isotopes are compared with experimental data. Quadrupole correlations play a minor role for Sn isotopes. They lead to a slight increase for mid-shell nuclei only which improves the agreement between calculation and experiment. Similar results have been obtained in a GCM calculation without projection in Ref [73]. The situation is somewhat different for Pb isotopes. Let us first examine the isotopes below  $^{208}\text{Pb}$ . For spherical mean fields, the radii vary nearly linearly with  $N$ . Allowing for deformation, a few neutron-rich isotopes around  $N = 108$  have an oblate ground state giving a larger radius compared to a spherical state. This is seen as a bump in Fig. 26. When dynamical correlations are included, the mean deformation of the correlated ground state decreases and their radii are intermediate between those of purely spherical and deformed mean-field calculations. Compared to experiment, there are some deviations from the linearity of the spherical mean field, but not as much as predicted by the GCM. Note that the appearance of a deformed mean-field ground states around  $^{186}\text{Pb}$  is very sensitive to the strength of the pairing interaction. Increasing it to  $-1250$  MeV fm $^3$ , as used in Ref. [74], pushes the oblate minimum up by a few 100 keV, leading to a spherical mean-field ground state for all Pb isotopes. Turning to the isotopes above  $^{208}\text{Pb}$ ,

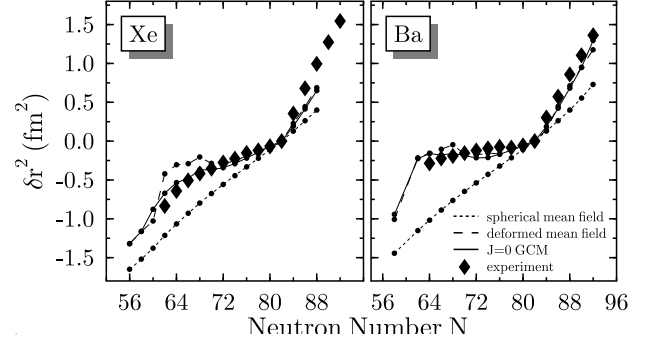


FIG. 27: Systematics of the isotopic shifts of the mean-square charge radii along the Xe ( $Z = 54$ ) and Ba ( $Z = 56$ ) isotopic chains. Isotopic shifts are with respect to the  $N = 82$  isotopes,  $^{136}\text{Xe}$  and  $^{138}\text{Ba}$ , respectively.

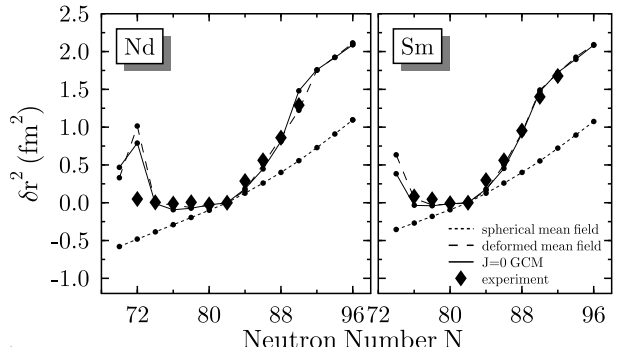


FIG. 28: Systematics of the isotopic shifts of the mean-square charge radii along the Nd ( $Z = 60$ ) and Sm ( $Z = 62$ ) isotopic chains. Isotopic shifts are with respect to the  $N = 82$  isotopes,  $^{142}\text{Nd}$  and  $^{144}\text{Sm}$ , respectively.

one sees a change in the slope of the isotope shifts in the data that is not reproduced by theory. Some authors explain the data by using an isospin dependence of the spin-orbit interaction [75, 76] different from that in SLy4 and which appears naturally in relativistic Lagrangians.

More drastic changes can be expected for nuclei further away from shell closures. The isotopic shifts in the Xe ( $Z = 54$ ), Ba ( $Z = 56$ ), and Nd ( $Z = 60$ ) and Sm ( $Z = 62$ ) isotopic chains. are shown in Figures 27 and 28 as examples of transitions from near-spherical to well-deformed ground states along isotopic chains. In all these cases, spherical mean-field calculations are obviously unable to describe the trends of the radii. With the exception of the  $N = 82$  isotopes, all nuclei in Figs. 27 and 28 are deformed, hence the static quadrupole correlations in mean-field ground states increase the radii on both sides of the  $N = 82$  shell, thereby decreasing the isotope shifts below and increasing them above. The up-bend above the  $N = 82$  shell seems to be fairly independent on the proton number and is always well-described. The difference between the SCMF ground state and the  $J = 0$  projected GCM ground state is in most cases quite small. Although dynamical correlations slightly increase them,

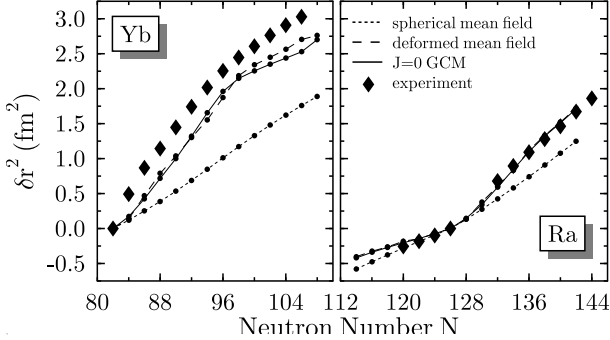


FIG. 29: Systematics of the isotopic shifts of the mean-square charge radii along the Yb ( $Z = 70$ ) and Ra ( $Z = 88$ ) isotopic chains. Isotopic shifts of Yb isotopes are with respect to the  $N = 82$  isotope  $^{152}\text{Yb}$ , in Ra with respect to the  $N = 126$  isotope  $^{214}\text{Ra}$ .

the isotopic shifts just above the magic number  $N = 82$  are always slightly underestimated. The situation is different below the  $N = 82$  shell. Going from  $Z = 54$  (Xe) to  $Z = 56$  (Ba) substantially increases the radii for mid-shell nuclei.

As a final example in Fig. 29, we show two isotopic chains that cross a transition from spherical to strongly deformed nuclei, Yb ( $Z = 70$ ) and Ra ( $Z = 88$ ). These are among the mid-shell chains for which the largest sets of data are available. A detailed discussion of the isotopic shifts in the Yb (and also the Pb) chain at the mean-field level can be found in Ref. [77]. The effect of deformation is clearly visible in the Yb chain. Static mean-field deformations bring the overall trend of the radii close to experiment, while dynamical correlations provide an additional small correction. An interesting feature is that we find an offset between our calculations and experiment for most nuclei except the neutron-magic  $^{152}\text{Yb}$ . The radius does not increase fast enough when going from  $N = 82$  to  $N = 84$ . This was already hinted in the case of the Xe, Ba, Nd and Sm isotopic chains, but it appears in a more pronounced way for Yb. There could be several sources for this discrepancy. Correlation modes that we do not consider here should play some role around magic numbers. Our results on mass systematics have also indicated that the  $N = 82$  gap is too large. As a consequence, the potential landscapes are too stiff, preventing the spreading of the collective ground state.

Compared to the Yb isotopes, the radii of the Ra isotopes vary on a smaller scale as shown in the right panel of Fig. 29. Static deformation increases the radii on both sides of the  $N = 126$  shell closure, in agreement with the available data. Adding dynamical correlations leaves the isotopic shifts practically unchanged.

## VIII. SUMMARY, DISCUSSION, AND OUTLOOK

Self-consistent mean-field (SCMF) methods provide the only microscopic nuclear model that can be applied to all nuclei up to the heaviest ones. In spite of their many successes, the SCMF models do not deliver nuclear masses with a satisfactory accuracy if phenomenological corrections are not added. We have studied how dynamical quadrupole correlations, calculated consistently from SCMF states, influence masses and charge radii. Using a numerical approximation to compute the matrix elements required for angular momentum projection and configuration mixing, it has been possible to calculate the quadrupole correlation energy for 600 even-even nuclei. We estimate a numerical uncertainty on correlation energies of at most 200 keV, which is acceptable for the purpose of our study.

SCMF masses determined with the Skyrme interaction SLy4 have two main wrong tendencies: a global drift with mass number, and arches between shell closures. Similar results have also been obtained for other Skyrme interactions. The drift with mass number is related to a slightly too small (approximately by 0.5 %) volume energy coefficient of the nuclear matter properties, that can be assumed to be an artifact of the common practice of fitting the force to a very limited set of nuclei. The mismatch can be easily removed by a perturbative refit of the particle-hole part of the effective mean-field interaction to a larger set of nuclear masses, while leaving the pairing interaction untouched.

The arches are obviously related to shell structure, and cannot be removed at the mean-field level by a perturbative refit of a given interaction. Including quadrupolar correlations brings a large improvement; they have the right qualitative behavior, and also the right order of magnitude. With the original Skyrme interaction SLy4, the amplitude of the arches is decreased. The residuals of the masses remain still large, but in particular mass differences around magic numbers become rather accurate. The improvements brought by correlations are smaller when included in a refit, but clearly are present for angular momentum projection; the overall improvement of the GCM is small and cannot be determined using a linear refit.

Surprisingly, the mismatch of masses related to shell effects is much more pronounced when residuals are plotted for isotopic chains as a function of the neutron number. In plots made as a function of the proton number or of the mass asymmetry, the residuals are much less structured.

The role of dynamical correlations for radii has many similarities with their role for masses. Correlations lead to an overall increase of radii that spoils the rms residuals for an interaction adjusted at the mean-field level. On the other hand, differences between radii are improved by correlations, the largest effect being obtained in mass regions where radii vary rapidly from isotope to the next, in particular for transitional nuclei and around magic num-

bers. The examples shown for isotopic shifts demonstrate that the dynamical quadrupole correlations indeed contain the right physics to improve the description of the ground states of transitional nuclei.

The aim of this paper was not to set up a new mass formula, microscopic and as accurate as the best available theories including phenomenological terms. This could only be done by refitting the effective interactions in both the mean-field and the pairing channels after the inclusion of correlations. Before to attack this formidable task, our more limited aim here was to determine the effect of correlations on residuals of binding energies and to see whether they have the right tendencies to remove the deficiencies of pure mean-field calculations. Our results for binding energies are encouraging in this respect. Energy differences are less sensitive to wrong global trends of effective interactions and the fact that they are significantly improved by correlations is a clear sign of the necessity to go beyond the mean field.

The spreading of the nuclear wave function over a large range of deformed mean-field states does not only influence binding energies. It has a large effect on other observables as well. We have examined a few representative examples of nuclear radii and isotopic shifts. Other observables require an extension of the present study to excited states.

What should be done to go further? We can distinguish several main roads which should ideally be followed in parallel but which all require new developments of different difficulties.

- From the analysis of mass residuals we conclude that the poor description of masses around heavy doubly-magic nuclei is due to a deficiency of the Skyrme energy functional, and is not primarily the manifestation of large missing correlations. This might be a hint that the present Skyrme energy functionals are not yet flexible enough. To improve the mean field used as a starting point, generalizations of the energy functional might be necessary. The fit of mean-field interactions should exclude  $N = Z$  nuclei, since the Wigner energy is large and not well known. Clearly, a fit protocol which takes into account only magic nuclei is not sufficient.
- the generalization of the present formalism to the study of low-lying excited states, in particular to the first  $2^+$  state and its decay by  $E2$  transitions to the ground state.
- the inclusion of additional collective modes. A nice feature of our study is that correlations seem to saturate and that the gain of energy for the ground state is small when introducing more correlations. However, in some mass regions, they should affect differently nuclei with different deformation topographies. Three modes seem the most natural ones looking to some deficiencies noticed in the present study. The octupole mode is certainly

missing in some heavy nuclei and should also be as important as the axial quadrupole mode near magic nuclei. The effect of triaxiality has to be tested in nuclei with coexisting mean-field prolate and oblate minima which, although already coupled even if only axial deformations are considered, could be more strongly linked through the triaxial plane. Finally, pairing has been treated within the Lipkin-Nogami approach, which is known to have deficiencies, in particular in the weak pairing regime. To include the pairing gap as a dynamical variable would certainly be more satisfactory.

- up to now, we have considered only even nuclei. It is clear that a more complete theory should also include odd ones. However, a treatment of odd nuclei at the same level of quality than even ones will require an extension of our model to break time-reversal invariance and axial symmetry. This work is underway but it is quite clear that the restoration of symmetries for odd nuclei will lead to a considerable increase of the computing time.
- the discussion of differences of energies and radii demonstrates that the introduction of quadrupole correlations brings in physics which is not included in self-consistent mean-field models and improves the systematics of ground state observables around shell closures. However, as we discussed several times in this paper, effective interactions have been adjusted at the mean-field level and are not adequate to include correlations. Nuclei whose masses were included in the determination of the interaction are over-bound by correlations. A linear refit of the mean-field part of the interaction permits to correct wrong tendencies of the interaction in a simple manner but is not sufficient for a quantitative study when configuration mixing is included. This is not surprising, since configuration mixing is very sensitive to the relative position of mean-field energy minima corresponding to different shapes. One therefore cannot avoid to readjust the effective interactions in both the mean-field and pairing channels simultaneously and with the inclusion of correlations.

Obviously, these five steps are not completely independent. For instance, several previous studies have shown that the excitation energy of the first excited  $2^+$  state is overestimated in spherical or near-spherical nuclei if only an axial quadrupole collective variable is considered. The variational space should probably enlarged in these cases by breaking the time-reversal invariance and introducing a cranking constraint. However, systematic studies with the present model are still required to determine which are the critical nuclei requiring an improved model.

From our study, one can also conclude that the absence of a Wigner term affects strongly the description of light nuclei, with a border between light and heavy

nuclei around mass 60. The linear refit of the effective interaction using the C-norm has also put into evidence critical nuclei. A first way to continue this study could be to use the C-norm to establish a larger list of critical nuclei. This will require to extend the data included in the refit of the interactions in order to lift the redundancy of the effective interaction parameters.

### Acknowledgments

We thank T. Duguet and W. Nazarewicz for their continuing interest in this work and many fruitful discussions on the interpretation of its results. We also thank B. Sabbey for help with various technical aspects

of this work, particularly on the binding energy fits. PHH thanks the Institute for Nuclear Theory for its hospitality during the initial stage of this work, MB thanks the Service de Physique Nucléaire Théorique at the Université Libre de Bruxelles for its warm hospitality during the final stage of this work. Financial support was provided by the U.S. Dept. of Energy under Grants DE-FG02-00ER41132 (Institute for Nuclear Theory) and W-31-109-ENG-38 (Argonne National Laboratory), the US National Science Foundation under grant PHY-0244453, and the Belgian Science Policy Office under contract PAI P5-07. The computations were performed at the National Energy Research Scientific Computing Center, supported by the U.S. Dept. of Energy under Contract No. DE-AC03-76SF00098.

- 
- [1] M. Bender, P.-H. Heenen, and P.-G. Reinhard, Rev. Mod. Phys. **75**, 121 (2003).
  - [2] F. Tondeur, S. Goriely, J. M. Pearson, and M. Onsi, Phys. Rev. **62**, 024308 (2000).
  - [3] P. Möller, J. R. Nix, W. D. Myers, and W. J. Swiatecki, Atom. Data Nucl. Data Tables **59**, 185 (1995).
  - [4] S. Goriely, F. Tondeur, and J. M. Pearson, At. Data Nucl. Data Tables **77**, 311 (2001).
  - [5] M. Samyn, S. Goriely, P.-H. Heenen, J. M. Pearson, and F. Tondeur, Nucl. Phys. **A700**, 142 (2002).
  - [6] O. Bohigas and P. Leboeuf, Phys. Rev. Lett. **88**, 092502 (2002); Phys. Rev. Lett. **88**, 129903(E) (2002).
  - [7] J. Barea, A. Frank, J. G. Hirsch, and P. Van Isacker, Phys. Rev. Lett. **94**, 102501 (2005).
  - [8] G. T. Garvey and I. Kelson, Phys. Rev. Lett. **16**, 197 (1966).
  - [9] G. T. Garvey, W. J. Gerace, R. L. Jaffe, I. Talmi, and I. Kelson, Rev. Mod. Phys. **41**, S1, (1969).
  - [10] E. Comay, I. Kelson, and A. Zidon, At. Data Nucl. Data Tables **39**, 235 (1988).
  - [11] A. Molinari and H. A. Weidenmüller, Phys. Lett. **B601**, 119 (2004).
  - [12] V. Velázquez, J. G. Hirsch, A. Frank, J. Barea, and A. Zuker, Phys. Lett. **B613**, 134 (2005).
  - [13] G. F. Bertsch, B. Sabbey, and M. Uusnäkki, Phys. Rev. C **71**, 054311 (2005).
  - [14] M. Bender, K. Rutz, P.-G. Reinhard, and J. A. Maruhn, Eur. Phys. J. **A7**, 467 (2000).
  - [15] I. Stetcu and C. W. Johnson, Phys. Rev. C **66**, 034301 (2002).
  - [16] S. Baroni, M. Armati, F. Barranco, R. A. Broglia, G. Colo', G. Gori, and E. Vigezzi, J. Phys. G: Nucl. Part. Phys. **30**, 1353 (2004).
  - [17] C. W. Johnson and I. Stetcu, Phys. Rev. C **66**, 064304 (2002).
  - [18] P. Ring and P. Schuck, *The Nuclear Many-Body Problem*, Springer Verlag, New York, Heidelberg, Berlin (1980).
  - [19] R. Rodriguez-Guzman, J. L. Egido, and L. M. Robledo, Nucl. Phys. **A709**, 201 (2002).
  - [20] M. Bender, H. Flocard and P.-H. Heenen, Phys. Rev. C **68**, 044321 (2003).
  - [21] K. Langanke and M. Wiescher, Rep. Prog. Phys. **64**, 1657 (2001).
  - [22] M. Arnould and S. Goriely, Phys. Rep. **384**, 1 (2003).
  - [23] M. Bender, G. F. Bertsch, and P.-H. Heenen, Phys. Rev. Lett. **94**, 102503 (2005).
  - [24] P. Bonche, H. Flocard, P.-H. Heenen, S. J. Krieger, and M. S. Weiss, Nucl. Phys. **A443**, 39 (1985).
  - [25] P. Bonche, H. Flocard, and P.-H. Heenen, Computer Phys. Comm. **171**, 49 (2005).
  - [26] D. Baye and P.-H. Heenen, J. Phys. **A19**, 2041 (1986).
  - [27] B. Gall, P. Bonche, J. Dobaczewski, H. Flocard, and P.-H. Heenen, Z. Phys. **A348**, 183 (1994).
  - [28] K. Rutz, J. A. Maruhn, P.-G. Reinhard, and W. Greiner, Nucl. Phys. **A590**, 680 (1995).
  - [29] E. Chabanat, P. Bonche, P. Haensel, J. Meyer, and R. Schaeffer, Nucl. Phys. **A635**, 231 (1998), Nucl. Phys. **A643**, 441(E) (1998).
  - [30] C. Rigollet, P. Bonche, H. Flocard, and P.-H. Heenen, Phys. Rev. C **59**, 3120 (1999).
  - [31] M. Bender, P. Bonche, and P.-H. Heenen, unpublished.
  - [32] M. V. Stoitsov, J. Dobaczewski, W. Nazarewicz, and P. Ring, Comp. Phys. Comm. **167**, 43 (2005).
  - [33] D. L. Hill and J. A. Wheeler, Phys. Rev. **89**, 1106 (1953).
  - [34] J. J. Griffin and J. A. Wheeler, Phys. Rev. **108**, 311 (1957).
  - [35] J. L. Egido and L.M. Robledo, in *Extended Density Functionals in Nuclear Physics*, G. A. Lalazissis, P. Ring, D. Vretenar [edts.], Lecture Notes in Physics No. 641 (Springer, Berlin, 2004), p. 269.
  - [36] M. Bender and P.-H. Heenen, Proceedings of ENAM'04, C. Gross, W. Nazarewicz, and K. Rykaczewski [edts.], in print.
  - [37] T. Duguet, P. Bonche, P.-H. Heenen, and J. Meyer, Phys. Rev. C **65**, 014310 (2002).
  - [38] R. Balian and E. Brézin, Il Nuovo Cimento B **64**, 37 (1969).
  - [39] K. T. R. Davies, H. Flocard, S. Krieger, and M. S. Weiss, Nucl. Phys. **A342**, 111 (1980).
  - [40] P. Bonche, J. Dobaczewski, H. Flocard, P.-H. Heenen, and J. Meyer, Nucl. Phys. **A510**, 466 (1990).
  - [41] A. Valor, P.-H. Heenen, and P. Bonche, Nucl. Phys. **A671**, 145 (2000).
  - [42] K. Hagino, G. F. Bertsch, and P.-G. Reinhard, Phys. Rev. C **68**, 024306 (2003).
  - [43] M. Bender, G. F. Bertsch, and P.-H. Heenen, Phys. Rev.

- C **69**, 034340 (2004).
- [44] A. Gozdz, K. Pomorski, M. Brack, and W. Werner, Nucl. Phys. **A442**, 26 (1985).
- [45] P.-G. Reinhard and K. Goeke, Rep. Prog. Phys. **50**, 1 (1987).
- [46] J. Libert, M. Girod, and J.-P. Delaroche, Phys. Rev. C **60**, 054301 (1999).
- [47] E. Kh. Yuldashbaeva, J. Libert, P. Quentin, and M. Girod, Phys. Lett. **B461**, 1 (1999).
- [48] L. Prochniak, P. Quentin, D. Samsoen, and J. Libert, Nucl. Phys. **A730**, 59 (2004).
- [49] P. Fleischer, P. Klüpfel, P.-G. Reinhard, and J. A. Maruhn, Phys. Rev. C **70**, 054321 (2004).
- [50] D. Baye and P.-H. Heenen, Phys. Rev. C **29**, 1056 (1984).
- [51] P.-G. Reinhard, D. J. Dean, W. Nazarewicz, J. Dobaczewski, J. A. Maruhn, and M. R. Strayer, Phys. Rev. C **60**, 014316 (1999).
- [52] M. Bender, P.-H. Heenen and P. Bonche, Phys. Rev. C **70**, 054304 (2004).
- [53] G. Audi, A. H. Wapstra, and C. Thibault, Nucl. Phys. **A729**, 337 (2003); the data file is available at <http://www-csadm.in2p3.fr/AMDC/masstable/Ame2003/mass.mas03>.
- [54] M. V. Stoitsov, J. Dobaczewski, W. Nazarewicz, S. Pittel, and D. J. Dean, Phys. Rev. C **68**, 054312 (2003).
- [55] S. Goriely, M. Samyn, P.-H. Heenen, J. M. Pearson, and F. Tondeur, Phys. Rev. C **66**, 024326 (2002).
- [56] M. Samyn, S. Goriely, and J. M. Pearson, Nucl. Phys. **718**, 653 (2003).
- [57] M. Samyn, S. Goriely, and J. M. Pearson, Nucl. Phys. **725**, 69 (2003).
- [58] S. Goriely, M. Samyn, M. Bender, and J. M. Pearson, Phys. Rev. C **68**, 054325 (2003).
- [59] M. Samyn, S. Goriely, M. Bender, and J. M. Pearson, Phys. Rev. C **70**, 044309 (2004).
- [60] S. Goriely, M. Samyn, J. M. Pearson, and M. Onsi, Nucl. Phys. **A750**, 425 (2005).
- [61] G. A. Lalazissis, T. Niksic, D. Vretenar, and P. Ring, Phys. Rev. C **71**, 024312 (2005).
- [62] V. Bernard and Nguyen Van Giai, Nucl. Phys. **A348**, 75 (1980).
- [63] K. Rutz, M. Bender, P.-G. Reinhard, J. A. Maruhn, Nucl. Phys. **A634**, 67 (1998).
- [64] If this article is accepted for publication in Phys. Rev. C, the file of correlation energies may be found at [http://ftp.aip.org/epaps/phys\\_rev\\_c](http://ftp.aip.org/epaps/phys_rev_c).
- [65] The SCMF wave functions calculated with the program **ev8** are available as well as the correlation energies are available at <http://gene.phys.washington.edu/ev8>.
- [66] S. Cwiok, W. Nazarewicz, and P.-H. Heenen, Phys. Rev. Lett. **83**, 1108 (1999).
- [67] P. A. Butler and W. Nazarewicz, Rev. Mod. Phys. **68**, 349 (1996).
- [68] N. Zeldes, T. S. Dumitrescu, and H. S. Köhler, Nucl. Phys. **A399**, 11 (1983).
- [69] D. Lunney, J. M. Pearson, and C. Thibault, Rev. Mod. Phys. **75**, 1021 (2003).
- [70] M. Bender, T. Cornelius, G. A. Lalazissis, J. A. Maruhn, W. Nazarewicz, and P.-G. Reinhard, Eur. Phys. J. **A14**, 23 (2002).
- [71] P.-H. Heenen, A. Valor, M. Bender, P. Bonche, H. Flocard, Eur. Phys. J. **A11**, 393 (2001).
- [72] I. Angeli, Atom. Data Nucl. Data Tables **87**, 185 (2004).
- [73] K. Bennaceur, P. Bonche, J. Meyer, C. R. Physique **4**, 555 (2003).
- [74] M. Bender, P. Bonche, T. Duguet, and P.-H. Heenen, Phys. Rev. C **69**, 064303 (2004).
- [75] M. M. Sharma, G. Lalazissis, J. König, and P. Ring, Phys. Rev. Lett. **74**, 3744 (1995).
- [76] P.-G. Reinhard and H. Flocard, Nucl. Phys. **A584**, 467 (1995).
- [77] S. Sakakihara and Y. Tanaka, Nucl. Phys. **A691**, 649 (2001).